

## Impurity doping: a novel strategy for controllable synthesis of functional lanthanide nanomaterials

Cite this: *Nanoscale*, 2013, 5, 4621

Daqin Chen and Yuansheng Wang\*

Many technological nanomaterials are intentionally 'doped' by introducing appropriate amounts of foreign elements into hosts to impart electronic, magnetic and optical properties. In fact, impurity doping was recently found to have significant influence on nucleation and growth of many functional nanocrystals (NCs), and provide a fundamental approach to modify the crystallographic phase, size, morphology, and electronic configuration of nanomaterials. In this feature article, we provide an overview of the most recent progresses in doping-induced control of phase structures, sizes, shapes, as well as performances of functional nanomaterials for the first time. Two kinds of impurity doping strategies, including the homo-valence ion doping and hetero-valence ion doping, are discussed in detail. We lay emphases on impurity doping induced modifications of microstructures and optical properties of upconversion (UC) lanthanide ( $\text{Ln}^{3+}$ ) NCs, but do not limit to them. In addition, we also illustrate the control of  $\text{Ln}^{3+}$  activator distribution in the core@shell architecture, which has recently provided scientists with new opportunities for designing and tuning the multi-color emissions of  $\text{Ln}^{3+}$ -doped UC NCs. Finally, the challenges and future perspectives of this novel impurity doping strategy are pointed out.

Received 22nd January 2013

Accepted 3rd March 2013

DOI: 10.1039/c3nr00368j

[www.rsc.org/nanoscale](http://www.rsc.org/nanoscale)

### 1 Introduction

During the past decade, functional nanomaterials have attracted great attention owing to their potential applications in biolabels, light-emitting devices, solar cells and catalysts, *etc.*<sup>1–5</sup>

It is well known that controlling the phase structure, size, shape and dimensionality of NCs is of fundamental and technological importance because of the strong correlation between these parameters and the physical/chemical characteristics, such as electronic, magnetic and optical properties. As a result, great efforts have already been devoted to developing new methods for the fabrication of these kinds of inorganic NCs, such as hydro/solvothermal method,<sup>6,7</sup> thermolysis,<sup>8,9</sup> chemical vapor deposition,<sup>10</sup> melt-salt method,<sup>11</sup> and the sonochemical route,<sup>12</sup>

State Key Laboratory of Structural Chemistry, Fujian Institute of Research on the Structure of Matter, Chinese Academy of Sciences, Fuzhou, 350002, P. R. China. E-mail: [yswang@fjirsm.ac.cn](mailto:yswang@fjirsm.ac.cn); Fax: +86-591-83705402; Tel: +86-591-83705402



Daqin Chen received his B.S. (2001) and M.S. (2004) degrees in Materials Science and Engineering from Central South University, China and his Ph.D degree (2008) in Condensed Matter Physics from Fujian Institute of Research on the Structure of Matter (FJIRSM), Chinese Academy of Sciences. He joined Prof. Yuansheng Wang's group in 2004, and now is a full Professor of Materials

Science at FJIRSM. His current research interest focuses on developing novel luminescent nanomaterials targeting at PV and LED applications. Since 2004, he has published over 40 first-author peer-reviewed papers in the field of impurity-doped optical nanomaterials.



Yuansheng Wang received his B.S. degree (1982) from University of Science and Technology of China (USTC), M.S. degree (1985) from Institute of Solid State Physics, CAS and Ph.D degree (1989) in Condensed Matter Physics from USTC. He has been a full Professor of Materials Science in Fuzhou University since 1999, and moved to Fujian Institute of Research on the Structure of

Matter, CAS as a research Professor in 2002, leading a group working in the field of photoelectric nano-materials. He has published over 150 peer-reviewed scientific papers.

*etc.* However, it still remains an open challenge to establish a suitable and facile synthetic methodology for the preparation of functional nanomaterials with easy control over phase, size, shape and dimensionality.

Doping, which involves the intentional incorporation of atoms or ions of suitable elements into host lattices, is one of the effective routes to endow electronic, magnetic and optical properties of many functional materials. An excellent example is the ruby solid-state laser whose gain medium is based on the  $\text{Cr}^{3+}$  doped  $\text{Al}_2\text{O}_3$  crystal. It is now generally anticipated that the performances of nanomaterials are different more or less from those of the same materials in bulk size.<sup>13</sup> Taking optical materials as an example, the size-dependent physical properties of host nanomaterials may significantly differ from those of the bulk ones and therefore affect the spectroscopic properties and luminescent dynamics of the optical activators in NCs.<sup>14–20</sup> For several decades, great endeavors have been devoted to investigate the impact of nanocrystalline structure, size and shape on the behaviors of dopants.<sup>21–23</sup> On the contrary, few works concerned the impurity doping-induced control over the growth and phase structure of functional NCs. In fact, impurity doping was recently found to have significant influence on the nucleation and growth of many functional nanomaterials, and provide a fundamental approach to modify the crystallographic phase, size, shape and electronic configuration of NCs.<sup>24–44</sup> In stark contrast to the conventional synthetic techniques that require stringent control over several experimental variables for tuning crystallite size and phase, the impurity-doping approach reviewed here requires modification of only a single variable (dopant concentration), while is able to tremendously improve our ability to control the formation of functional NCs. Therefore, understanding the underlying mechanism and extending the preparation method for functional NCs with precise control of their crystalline phases, sizes and shapes through impurity doping would enhance their physical/chemical performance and enable their use in a number of important applications.

In this feature article, we try to make a general survey on the most recent progresses in doping-induced control of phase structures, sizes, shapes as well as properties of functional nanomaterials for the first time. Two kinds of impurity doping strategies, homo-valence ion doping and hetero-valence ion doping, are discussed in detail. We will lay emphases on impurity-doping induced modifications of the microstructures and optical properties of UC NCs, but not limit to them. UC is an anti-Stokes process where long wavelength exciting radiation is converted into shorter wavelength emitting light *via* a two- or multi-photon absorption mechanism.<sup>45</sup> Recently, lanthanide doped monodisperse UC NCs have been developed as a new category of luminescent labels that have become promising alternatives to the organic fluorophores and quantum dots applied in biological assays and medical imaging, owing to their unique optical characteristics, such as sharp emission bands, long luminescent lifetimes (micro- to milli-seconds), good photostability, low background autofluorescence, as well as low toxicity.<sup>46–51</sup> Besides, we will also illustrate the control of  $\text{Ln}^{3+}$  activator distribution in the core@shell architecture, which has recently provided scientists with new opportunities for

designing and tuning the multi-color emissions of UC NCs. Finally, the challenges and perspectives of this novel impurity-doping strategy are pointed out.

## 2 Doped NCs and doping routes

It is noteworthy that the definition of doping for the doped NCs and for the semiconductor industry is largely different. In the traditional semiconductor industry, doping means introduction of a trace amount of impurities into extremely pure semiconductors. When dopant concentration is on the order of 1 per 10 000 atoms, the doping is referred to as heavy or high. If this description is applied to the doped NCs, even a minimum level of doping, one single dopant ion in an individual NC shall be called heavy doping since the number of ions contained in a NC is generally less than 10 000. In many publications of doped NCs, doping simply refers to the incorporation of dopant ions into the host crystal lattices. The dopant concentrations of the doped NCs can be as high as a few percent, and in some cases, even over fifty percent, which in fact form alloyed NCs.<sup>24,25,36–38</sup> The concept of doping that is generally used for doped NCs is adopted in the present review.

To incorporate impurities into the host lattice, a common route is to adopt the doping ions with the same valence and the similar radii to the ones in the hosts. When the dopants have different valence to the substituted host ions, extra vacancies or interstitial ions will be introduced into the host lattices during the nucleation and growth because of the requirement of charge compensation. The possible changes in the crystal lattice after impurity doping are schematically illustrated in Fig. 1. For homo-valence ion doping, the crystal lattice will contract or expand when small- or large-size impurities are doped to substitute the host ions (Fig. 1a and b). For hetero-valence ion doping, the variations of crystal lattice are complex due to the requirement of extra vacancy or interstitial ions to compensate charge (Fig. 1c and d). In addition, another possible doping route is to directly incorporate the impurities into the interstitial positions (Fig. 1e).

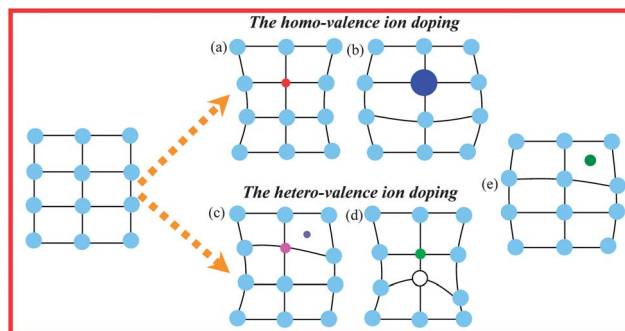


**Fig. 1** Schematically illustrating the possible impurity doping routes in the host lattice: (a) substitution by a small homo-valence dopant, (b) substitution by a large homo-valence dopant, (c) combination of substitution by a hetero-valence dopant and interstitial occupation by an extra ion for charge compensation, (d) combination of substitution by a hetero-valence dopant and vacancy occupation for charge compensation, and (e) interstitial occupation by a small dopant.

### 3 Doping of homo-valence ions

#### 3.1 Doping of homo-valence ions into UC fluoride NCs

The selection of appropriate host materials is essential for realizing favorable optical performance, such as high UC efficiency and controllable emission profile, for the doping  $\text{Ln}^{3+}$  ions. Hexagonal  $\beta\text{-NaYF}_4$  co-doped with  $\text{Yb}^{3+}/\text{Er}^{3+}(\text{Tm}^{3+})$  is regarded as the most efficient green (blue) upconversion (UC) phosphor.<sup>52</sup> Unfortunately,  $\text{NaYF}_4$  host exists in two phase structures, cubic ( $\alpha$ ) and hexagonal ( $\beta$ ), and the UC efficiency of  $\alpha\text{-NaYF}_4$  is much lower than that of  $\beta\text{-NaYF}_4$ .<sup>52</sup> Recently, Liu *et al.* described a system in which lanthanide doping can be used to control the growth of  $\text{NaYF}_4$  NCs, making it possible to simultaneously tune the size, crystallographic phase and optical properties of the resulting materials.<sup>24</sup> Without deliberate introduction of  $\text{Gd}^{3+}$  ions, transmission electron microscope (TEM) image of the  $\text{Yb}/\text{Er}:\text{NaYF}_4$  sample prepared in an aqueous solvent at 200 °C for 2–10 h shows two distinct particle morphologies that include small cubic nanocubes and large hexagonal nanorods (Fig. 2a–e). However, in the presence of  $\text{Gd}^{3+}$  dopants (30 mol%), the cubic-to-hexagonal phase conversion is clearly complete after only 2 h under identical reaction conditions (Fig. 2f). The dramatic shortening of reaction time on phase transformation was further confirmed by repeated doping experiments with 45 mol% and 60 mol% of  $\text{Gd}^{3+}$ . In all cases, the complete conversion of cubic to hexagonal phase occurred after 2 h, resulting in formation of highly uniform nanorods (Fig. 2g and h). In addition, nanorods with gradually decreasing sizes are formed (Fig. 2f–h) with increasing of  $\text{Gd}^{3+}$

dopant content (30, 45, 60 mol%). Density functional theory (DFT) calculations indicate that the formation energy per atom in hexagonal structure increases by about 0.07 eV when  $\text{Y}^{3+}$  is replaced by  $\text{Gd}^{3+}$ , indicating that  $\text{NaGdF}_4$  is more energetically stable than  $\text{NaYF}_4$ . The calculations are consistent with the experimental observations showing that an increase of  $\text{Gd}^{3+}$  dopant content in the  $\text{NaYF}_4$  host favors the formation of hexagonal phase NCs. The size evolution of  $\text{NaYF}_4$  NCs can be partly attributed to the strong effect of the  $\text{Gd}^{3+}$  dopants on crystal growth rate through surface charge modification. DFT calculation shows that the electron charge density of the crystal surface increases after a  $\text{Gd}^{3+}$  ion substitutes the  $\text{Y}^{3+}$  one in the crystal lattice. The change of electron charge density on the surface of NCs can substantially slow the diffusion of negatively charged  $\text{F}^-$  ions to the surface owing to an increase in charge repulsion, which results in a tunable reduction of the  $\text{NaYF}_4$  NCs size (Fig. 2j).

Similarly, we have successfully prepared  $\text{NaYb}_{1-x}\text{Gd}_x\text{F}_4$  ( $0 \leq x \leq 1$ ) NCs by a facile solvothermal method for the first time.<sup>25</sup> The addition of  $\text{Gd}^{3+}$  into  $\text{NaYbF}_4$  NCs also prompted the phase conversion from cubic to hexagonal, and the mean size of hexagonal NCs was monotonously reduced with increasing of  $\text{Gd}^{3+}$  content, similar to the case of  $\text{Gd}^{3+}$  doped  $\text{NaYF}_4$ . Further experiments evidenced that the addition of other lanthanide ions with radius larger than  $\text{Yb}^{3+}$  has a similar effect as that of  $\text{Gd}^{3+}$ . Importantly, by doping appropriate active lanthanide ions into the monodisperse  $\text{NaYb}_{0.4}\text{Gd}_{0.6}\text{F}_4$  nanorods, they exhibited multi-functionality, *i.e.*, tunable down- and up-conversion emissions as well as proper paramagnetism.

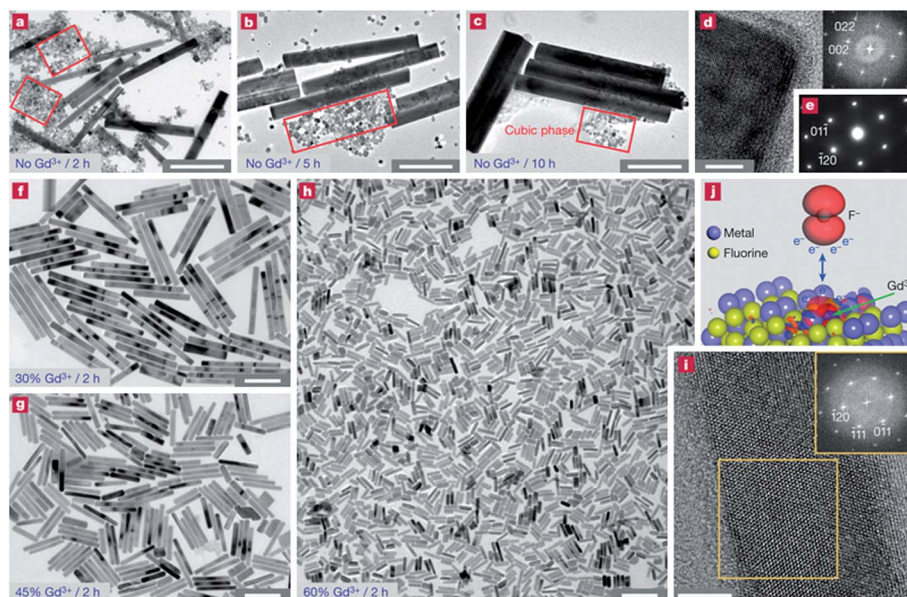


**Fig. 2** (a–c) TEM micrographs of  $\text{Yb}/\text{Er}$  (18/2 mol%):  $\text{NaYF}_4$  products obtained after heating for 2, 5 and 10 h at 200 °C in the absence of  $\text{Gd}^{3+}$  dopants. Formation of the cubic phase is partially marked by red squares. (d) High-resolution TEM image and the corresponding Fourier-transform diffractogram (inset) of a cubic nanocube. (e) Selected area electron diffraction pattern of a hexagonal nanorod. (f–h) TEM micrographs of the  $\text{Yb}/\text{Er}$  (18/2 mol%):  $\text{NaYF}_4$  products obtained after heating for 2 h at 200 °C in the presence of 30, 45 and 60 mol%  $\text{Gd}^{3+}$  dopants, respectively. (i) High-resolution TEM image and the corresponding Fourier-transform diffractogram (inset) of a hexagonal nanorod shown in (h). (j) DFT calculation showing the change of surface charge density caused by replacing the  $\text{Y}^{3+}$  in the host lattice with a  $\text{Gd}^{3+}$  ion. The red shading around the  $\text{Gd}^{3+}$  ion denotes the increased negative charges upon ion exchange. Scale bars are 500 nm for panels (a–c), 200 nm for panels (f–h) and 5 nm for panels (d) and (i). Reproduced with permission from ref. 24. © 2010 Nature Publishing Group.



Doping  $\text{Ln}^{3+}$  ions with large ionic radius (such as  $\text{La}^{3+}$ ,  $\text{Ce}^{3+}$ ,  $\text{Pr}^{3+}$ ,  $\text{Nd}^{3+}$  and  $\text{Sm}^{3+}$ ) can induce phase transition from orthorhombic to the hexagonal phase of  $\text{EuF}_3$  NCs. Meanwhile, the size of the product can be reduced dramatically with increasing of  $\text{Ln}^{3+}$  dopant content.<sup>26</sup> Generally,  $\text{Ln}^{3+}$  ions with a larger radius have a lower energy barrier to form the hexagonal phase  $\text{LnF}_3$  NCs, and the larger the radius of the  $\text{Ln}^{3+}$ , the larger the electron charge density on the surface of NCs. Therefore, when  $\text{Eu}^{3+}$  ions are substituted by  $\text{Ln}^{3+}$  ions with larger radius, hexagonal  $\text{EuF}_3$  was easily formed. Meanwhile, the increase of surface electron charge density can dramatically slow the diffusion of  $\text{F}^-$  ions to the surface of  $\text{EuF}_3$  because of the increase of charge repulsion, which induces the formation of small-sized NCs.

Yang *et al.* demonstrate that lanthanide doping not only works as sensitizer and activator, but also plays an important role to facilitate the growth of UC NCs.<sup>27</sup> With the introduction of the dopants of  $\text{Ho}^{3+}$ ,  $\text{Er}^{3+}$ , or  $\text{Yb}^{3+}$ , the growth of  $\text{Ba}_2\text{LaF}_7$  NCs was obviously facilitated to a certain size within a shorter reaction time. A similar phenomenon was also observed for  $\text{LaF}_3$  NCs. They concluded that  $\text{Ln}^{3+}$  (e.g.,  $\text{Ho}^{3+}$ ,  $\text{Er}^{3+}$ , or  $\text{Yb}^{3+}$ ) with smaller radius can reduce the nucleation energy and lead to heterogeneous nucleation, which favors the growth of  $\text{Ba}_2\text{LaF}_7$  or  $\text{LaF}_3$  NCs quickly.

The influence of  $\text{Li}^+$  doping on the phase structures and morphologies of  $\text{NaYF}_4$  NCs was investigated recently.<sup>28</sup> In the hexagonal lattice,  $\text{Na}^+$  and  $\text{Y}^{3+}$  ions randomly occupy the same lattice sites due to their similar ionic radius. When a small amount of  $\text{Li}^+$  is doped into the lattice, they may locate in either the lattice sites by substituting  $\text{Na}^+$  ions or interstitial ones. When 20 mol% of  $\text{Li}^+$  was doped, hexagonally structured  $\text{NaYF}_4$  nanorods were retained (Fig. 3a). With  $\text{Li}^+$  content increasing to 40–60%, the NCs changed from hexagonally structured nanorods to cubic structured nanospheres (Fig. 3b). When a

relatively large amount of  $\text{Li}^+$  was doped into the crystal structure, the electron cloud of the ions was distorted due to the imbalance of the crystal lattice caused by the size mismatch after the  $\text{Li}^+$  substitution. Due to the steric effect,  $\text{Y}^{3+}$  cannot coordinate with  $\text{F}^-$  of the same number as in the NCs before  $\text{Li}^+$  doping, which causes the imbalance in hexagonal crystal lattice and the change to cubic phase. Once the amount of  $\text{Li}^+$  ions was further increased, due to the size mismatch, the imbalance in the NC structure caused by the  $\text{Li}^+$  doping became more serious and the phase transition to tetragonal parallelogram-shaped  $\text{LiYF}_4$  occurred (Fig. 3c).

From the opposite point of view, Lin *et al.* studied the influence of  $\text{Na}^+$  doping on the size and morphology of  $\text{Yb}/\text{Er}:\text{LiYF}_4$  NCs.<sup>29</sup> It was found that the size and morphology of the as-prepared products were closely related to the doping content of  $\text{Na}^+$  in the  $\text{LiYF}_4$  host. Considering that ionic radius  $r(\text{Li}^+) < r(\text{Na}^+)$ , size mismatch can cause the imbalance of the crystal lattice when  $\text{Na}^+$  was doped into  $\text{LiYF}_4$  host. After introducing  $\text{Na}^+$  impurities, the crystal unit cell of  $\text{LiYF}_4$  expanded and the imbalance in  $\text{Na}^+$ -doped  $\text{LiYF}_4$  NCs became more serious when  $\text{Na}^+$  content was further increased. To offset this imbalance, the crystal phase tended to transfer to cubic  $\text{NaYF}_4$ . As a result, the morphologies of  $\text{LiYF}_4$  NCs changed from rhombus to nanospheres with increasing  $\text{Na}^+$  content from 0 to 30 mol% (Fig. 3d–g). In addition, the doping of  $\text{Na}^+$  in  $\text{Yb}/\text{Er}:\text{LiYF}_4$  NCs not only affects their morphology but also influences their UC properties. Selective enhancement of red emission can be achieved by increasing of  $\text{Na}^+$  content, which leads to the color-tunable UC emissions for the as-prepared products (Fig. 3h). When  $\text{Na}^+$  ions were doped into the  $\text{LiYF}_4$  host, the crystal lattice will be slightly expanded, and the distance between sensitizer ions ( $\text{Yb}^{3+}$ ) and activator ones ( $\text{Er}^{3+}$ ) will be enlarged. Thus, the energy transfer from  $\text{Yb}^{3+}$  to  $\text{Er}^{3+}$  will be influenced, and eventually affected the UC colors.

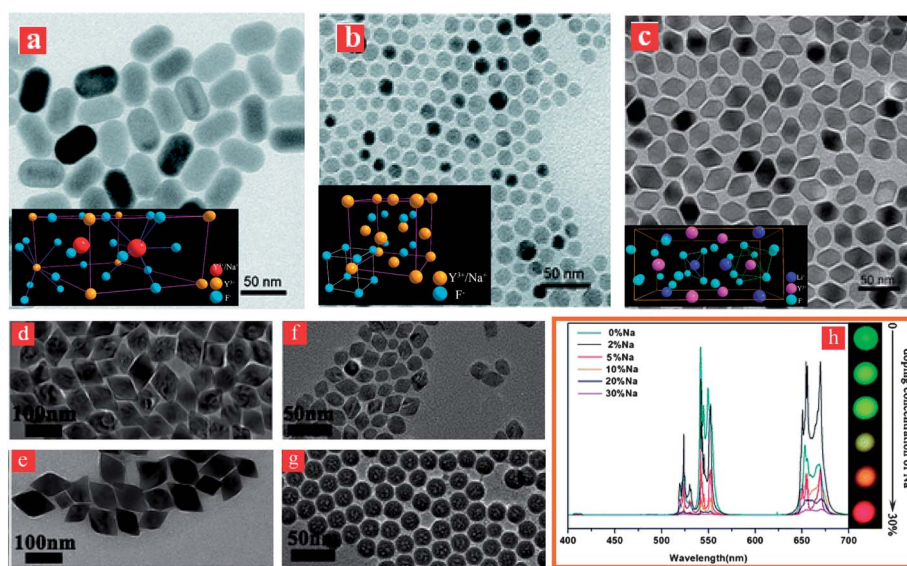


**Fig. 3** TEM micrographs of (a–c)  $\text{Li}^+$  doped  $\text{Na}_{1-x}\text{YF}_4$  ( $x = 0.2, 0.6$  and  $0.8$ ) NCs and (d–g)  $\text{Na}^+$  doped  $\text{Li}_{1-y}\text{YF}_4$  ( $y = 0, 0.02, 0.1$  and  $0.3$ ) NCs; insets of (a–c) are the crystal structures of the corresponding NCs; (h) UC emission spectra and corresponding luminescent photos of  $\text{Yb}/\text{Er}:\text{Li}_{1-y}\text{Na}_y\text{YF}_4$  NCs ( $0 \leq y \leq 0.3$ ). Reproduced with permission from ref. 28 and 29 © 2011 American Chemical Society. © 2012 Royal Society of Chemistry.

All the above-mentioned cases are related to the substitution of host ions by cationic dopants. Recently, we investigated the doping behaviors of anionic ions into the hosts. Adopting the pre-formed cubic phase  $\text{MF}_2$  ( $M = \text{Ca}, \text{Sr}, \text{Ba}$ ) NCs as seeds in the oleic acid and 1-octadecene mixed solution, the introduced  $\text{Cl}^-$  ions will be easily incorporated into the host to replace  $\text{F}^-$  ones and subsequently induce the formation of tetragonal phase  $\text{MFCl}$  NCs when the  $\text{Cl}^-$  dopant content is high enough.<sup>30</sup> Remarkably, the UC emissions of  $\text{Yb/Er:MFCl}$  NCs are found to be greatly intensified compared with those of the well-reported  $\text{Yb/Er:MF}_2$  with the same size and shape, owing to lower non-radiative deactivation probability of  $\text{Ln}^{3+}$  in  $\text{MFCl}$  than that in  $\text{MF}_2$ .

### 3.2 Doping of homo-valence ions into oxide NCs

Ceria ( $\text{CeO}_2$ ) nanoparticles are one of the key abrasive materials for chemical-mechanical planarization of advanced integrated

circuits. However, ceria nanoparticles synthesized by existing techniques are irregularly faceted, and they scratch the silicon wafers and increase defect concentrations. Recently, Wang *et al.* evidenced that polyhedral  $\text{CeO}_2$  nanoparticles can be easily converted into nanospheres by doping  $\text{Ti}^{4+}$  ions<sup>31</sup> which play an important role in stabilizing a specific crystallographic phase (Fig. 4). They doped the ceria system with titanium, using flame temperatures that facilitate crystallization of the ceria yet retain the titania in a molten state. In conjunction with molecular dynamics simulation, they show that under these conditions, the inner ceria core evolves in a single-crystal spherical shape without faceting, because throughout crystallization it is completely encapsulated by a molten 1 to 2 nanometer shell of titania that, in liquid state, minimizes the surface energy (Fig. 5).

Zinc oxide ( $\text{ZnO}$ ) can be synthesized into a variety of morphologies including nanowires, nanorods, tetrapods, nanobelts, nanoflowers, nanoparticles, *etc.*, and  $\text{ZnO}$  NCs are promising candidates for nanoelectronics and photonics. It is well known that  $\text{ZnO}$  transforms from fourfold wurtzite (B4) to six-fold coordinated rocksalt (B1) structure with the pressure raised from an ambient condition. Li *et al.* recently used DFT calculations to study impurities doped  $\text{ZnO}$  NCs and found that the transition pressure from B4 phase to B1 phase of  $\text{ZnO}$  always decreases through doping different types of transition metals such as V, Cr, Mn, Fe, Co, and Ni, but the phase transition path is not affected by the dopants.<sup>32,33</sup> This is consistent with the available experimental results in Mn-doped  $\text{ZnO}$  and Co-doped one. Doping in  $\text{ZnO}$  causes the lattice distortion, which causes the decrease of the bulk modulus and accelerates the phase transition. Notably, for V-doped and Cr-doped  $\text{ZnO}$ , the magnetism is enhanced by phase transition from B4 to B1, however for Mn-doped, Fe-doped, Co-doped, and Ni-doped  $\text{ZnO}$ , B1 phase shows weaker magnetic moment than B4 phase, which can be explained by the amount of charge transferred from the doped ions to  $\text{O}^{2-}$  ones. These results provide a theoretical basis for the doping approach to control the structures and properties of  $\text{ZnO}$  and other similar materials.

Another example is dopant-induced shape evolution of  $\text{ZnO}$  colloidal NCs. The creation of  $\text{Mg}^{2+}$ -doped  $\text{ZnO}$  NCs provides an excellent example. Depending on the molar ratio of dopant precursor in the reagents,  $\text{Mg}^{2+}$ -doped NCs with well-defined shapes, from tetrapods to ultrathin nanowires (Fig. 6), which exhibit tunable optoelectronic properties, are obtained for the first time by Ye *et al.*<sup>34</sup>  $\text{Mg}^{2+}$  dopants play an important role in the primary growth stage, and cause initial growth seeds having diverse crystallographic structures, which are critical for the generation of doped NCs with different shapes. This “greener” synthetic scheme can be extended to other dopant systems and provides an attractive and effective strategy for fabricating doped  $\text{ZnO}$  NCs with interesting compositional and spatial complexity.

Magnetic NCs are a class of nanostructured materials of current interest, mainly due to their advanced technological and medical applications. Among various magnetic NCs, magnetite ( $\text{Fe}_3\text{O}_4$ ) nanoparticles are arguably the most extensively investigated. Recently, highly monodisperse  $\text{Ln}^{3+}$ -doped

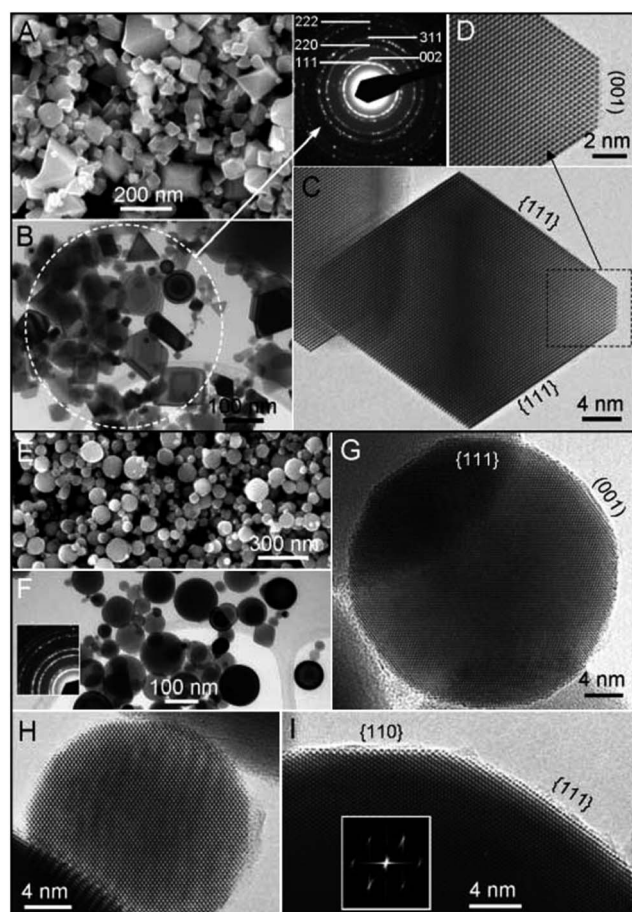


**Fig. 4** (A to D) Microstructure of  $\text{CeO}_2$  nanoparticles without  $\text{Ti}^{4+}$  doping: (A) scanning electron microscopy (SEM) image, (B) low magnification TEM image, and (C and D) high-resolution TEM images of the ceria NCs with faceted shapes. The inset between (A) and (D) is an electron diffraction pattern from the area circled in (B). (E to I) Microstructure of  $\text{CeO}_2$  nanospheres doped with 6 mol% of  $\text{Ti}^{4+}$ : (E) SEM image, (F) low-magnification TEM micrograph, and [(G) to (I)] high-resolution TEM images of the ceria NCs, showing their spherical shape and single-crystal structure. The inset in (F) is an electron diffraction pattern recorded from the area, showing the cubic ceria structure of the sample. The inset in (I) is a fast Fourier transform of the high-resolution TEM image. Reproduced with permission from ref. 31. © 2006 American Association for the Advancement of Science.



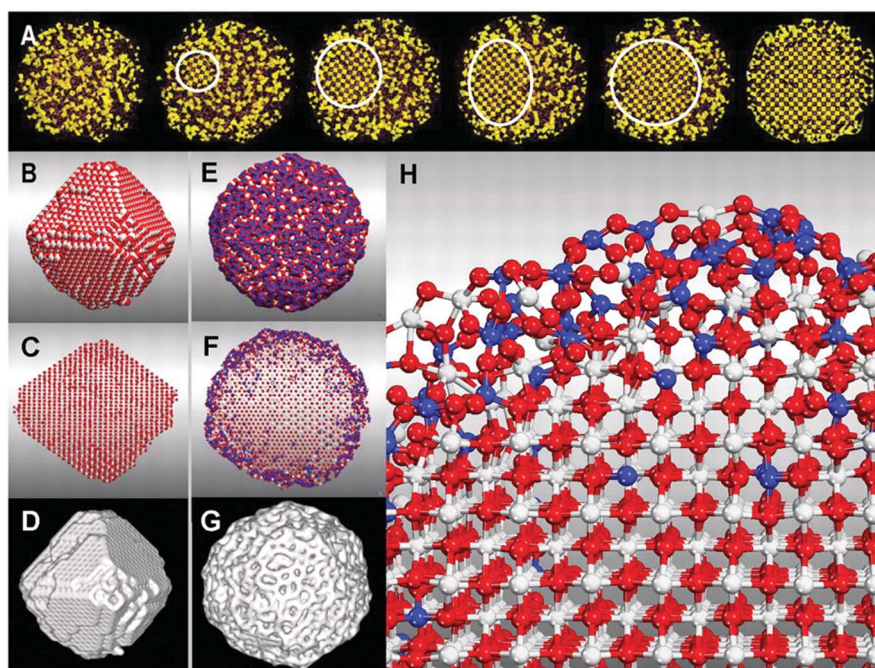


**Fig. 5** (A) Images taken during a crystallization simulation ( $\text{Ti}^{4+}$ -doped  $\text{CeO}_2$ ), showing the initial amorphous precursor (left), evolution, and growth of the seed (circled) to the fully crystalline  $\text{CeO}_2$  NC with amorphous  $\text{TiO}_2$  shell (right). (B to D) Non-doped nanoparticle. (E to G)  $\text{Ti}^{4+}$ -doped  $\text{CeO}_2$  nanosphere. (H) Enlarged segment of the  $\text{Ti}^{4+}$ -doped nanosphere. [(B) and (E)] Sphere model representation of the ionic positions. [(C) and (F)] Side view with smaller spheres to view through the nanoparticle. [(D) and (G)] Surface rendered model.  $\text{Ce}^{4+}$  is colored white;  $\text{Ti}^{4+}$  is blue, and  $\text{O}^{2-}$  is red. The nanoparticles are about 7 to 8 nm in diameter. All images show actual ionic positions and are not schematics. Reproduced with permission from ref. 31. © 2006 American Association for the Advancement of Science.

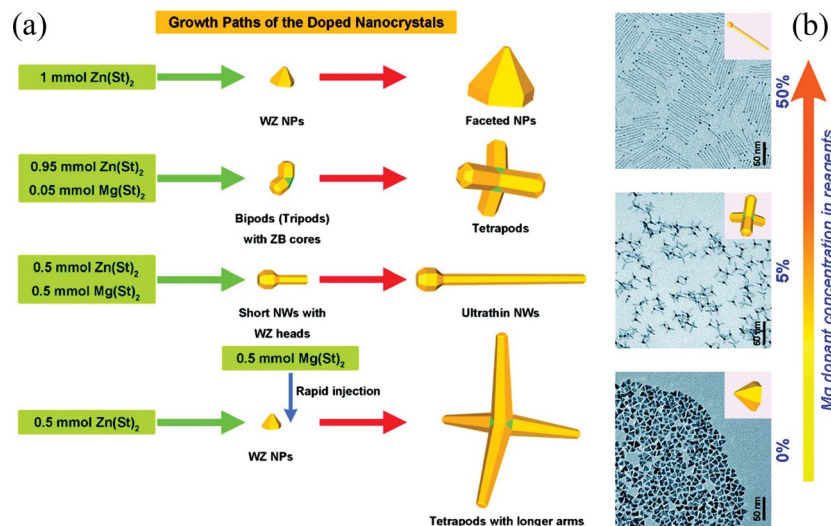


**Fig. 6** (a) Schematic illustration of the impact of  $\text{Mg}^{2+}$  dopants on the shapes of ZnO NCs; (b) representative TEM micrographs of ZnO NCs doped with 0%, 5% and 50%  $\text{Mg}^{2+}$  ions, emphasizing the shape evolution of colloidal NCs due to the increasing Mg dopant contents in the reagents (highlighted by the arrow). Reproduced with permission from ref. 34. © 2010 American Chemical Society.

magnetite nanoparticles have been successfully prepared by thermally decomposing a mixture of acetylacetonates of  $\text{Fe}^{3+}$  and those of  $\text{Ln}^{3+}$  ( $\text{Ln} = \text{Sm}, \text{Eu}, \text{Gd}$ ). In contrast to the undoped, superparamagnetic magnetite nanoparticles prepared under identical conditions, these  $\text{Ln}^{3+}$ -doped NCs are unquestionably ferromagnetic at room temperature, possibly ascribing to an

increase in magnetic anisotropy of the doped NCs after the introduction of  $\text{Ln}^{3+}$  ions.<sup>35</sup>

In a word, series of experiments evidence that the homo-valence ions doping exhibits great potential in controlling the phase structures, sizes, shapes as well as properties of many functional nanomaterials. Notably, although the dopants and the

substituted host ions usually have similar electronic configurations, the role of impurity doping on changing the nucleation energy barriers as well as the growth kinetics of NCs is quite striking.

## 4 Doping of hetero-valence ions

### 4.1 Doping of hetero-valence ions into UC fluoride NCs

Notably, different to the case of the homo-valence ions doping, the hetero-valence ions doping introduces extra vacancies or interstitial ions into the host lattice during the nucleation and growth because of the requirement of charge compensation. In this case, substantial modification of phase structure, composition, size and shape of NCs is expected.

The phase relationships between alkaline-earth bi-fluorides ( $\text{MF}_2$ ,  $\text{M}^{2+} = \text{Ca}^{2+}$ ,  $\text{Sr}^{2+}$ ,  $\text{Ba}^{2+}$ ) and lanthanide tri-fluorides ( $\text{LnF}_3$ ,  $\text{Ln}^{3+} = \text{La}^{3+}$ – $\text{Lu}^{3+}$ ,  $\text{Y}^{3+}$ ) have been of immense interest owing to the possible applications of their mixed fluorides as the optical hosts and ion selective electrodes.<sup>53,54</sup> The high-temperature phase equilibria relations of the  $\text{MF}_2$ – $\text{LnF}_3$  systems have been well studied and found to usually consist of cubic fluorite-type and hexagonal tysonite-type disordered solid solutions.<sup>55,56</sup> On the  $\text{MF}_2$  side, high content of  $\text{LnF}_3$ , exceeding in some cases 50 mol%, can be incorporated into  $\text{MF}_2$  crystals without changing their fluorite structure. On the  $\text{LnF}_3$  side, the systems are characterized by the formation of hexagonal solid solutions with the tysonite structure, which are stable with approximately up to 15–20 mol%  $\text{MF}_2$ .<sup>55</sup> Therefore, the  $\text{MF}_2$ – $\text{LnF}_3$  fluorides are suitable hosts for investigating the impact of hetero-valence dopants on the nucleation and growth of NCs.

Recently, we reported for the first time the hetero-valence dopants (lanthanide ions) induced size-control in alkaline-earth fluorides ( $\text{MF}_2$ ,  $\text{M} = \text{Ca}$ ,  $\text{Sr}$ ,  $\text{Ba}$ ).<sup>36</sup> The selection of  $\text{MF}_2$  as the doping host was motivated by their high solubility for trivalent lanthanide ions as well as their low phonon energy, which favors suppression of nonradiative losses and thereby improves the luminescence of the optically active dopants. We evidenced that using  $\text{Ln}^{3+}$  ions to substitute for divalent alkaline-earth ones in  $\text{MF}_2$  NCs allows products with uneven size and shape to be easily modified into monodisperse nanospheres with ultra-small sizes of  $\sim 5$  nm in a solution system (Fig. 7a and 7b). The possible mechanism is as follows: each substitution of  $\text{M}^{2+}$  by  $\text{Ln}^{3+}$  in  $\text{MF}_2$  requires an extra  $\text{F}^-$  for charge compensation, and the introduction of such  $\text{F}^-$  ions into the grain surface may induce transient electric dipoles with their negative poles outward. These transient electric dipoles hinder the diffusion of  $\text{F}^-$  ions (which are needed for crystal growth) from the solution to the grain surface, thus retarding the growth of  $\text{MF}_2$  (Fig. 7c). As an evidence to verify the above mechanism from the reverse angle, we also found that the growth of lanthanide tri-fluoride ( $\text{LnF}_3$ ) NCs is obviously promoted by doping of low content (5 mol%) alkaline-earth ions. It is believed that replacement of  $\text{Ln}^{3+}$  by  $\text{M}^{2+}$  generates cation vacancies, forming transient electric dipoles with positive poles pointing outward on the grain surface which accelerates diffusion of  $\text{F}^-$  ions from solution to grain (Fig. 7c). Evidently, the  $\text{Ln}^{3+}$ -doped  $\text{MF}_2$  NCs exhibit bifunctionality, *i.e.*, tunable UC luminescence and proper paramagnetism, and therefore may find potential applications in the biological field.

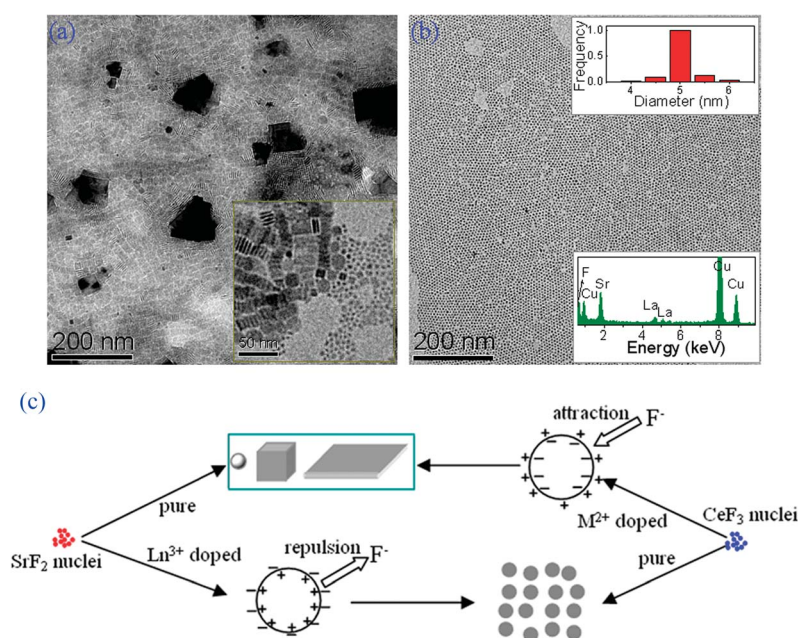


**Fig. 7** (a) TEM micrograph of pure (un-doped)  $\text{SrF}_2$  NCs; inset shows an enlarged image of small NCs with multiplex shapes. (b) TEM micrograph of 20 mol%  $\text{La}^{3+}$ -doped  $\text{SrF}_2$  nanospheres; the upper inset shows a histogram of the particle size distribution and the lower one the EDS spectrum taken from the nanospheres (Cu signals come from the copper grid). (c) Schematic illustration of the modifications of impurity doping on the size and shape of  $\text{SrF}_2$  and  $\text{CeF}_3$  NCs. Reproduced with permission from ref. 36. © 2010 American Chemical Society.



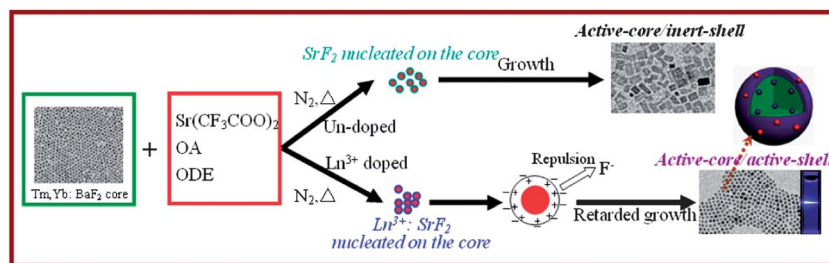


**Fig. 8** Schematic illustration of the influence and related mechanism of  $\text{Ln}^{3+}$  doping on the size of  $\text{BaF}_2@\text{SrF}_2$  core/shell NCs. Reproduced with permission from ref. 37. © 2012 Royal Society of Chemistry.

Similarly, this strategy can be used to control the size of core@shell NCs. For example, we demonstrate the  $\text{Ln}^{3+}$  dopant-induced formation of ultrasmall uniform  $\text{Ln}^{3+}:\text{BaF}_2@\text{Ln}^{3+}:\text{SrF}_2$  active-core@active-shell architectures (Fig. 8).<sup>37</sup> The  $\text{Ln}^{3+}$  ions doped in the shell are evidenced to play a key role to retard the growth of the core@shell NCs. Particularly, adopting  $\sim 3$  nm Yb/Tm: $\text{BaF}_2$  NCs as cores prepared by a solvothermal reaction, growth of Nd: $\text{SrF}_2$  shells is successfully induced on the surfaces of these cores through a thermal decomposition process, forming  $\sim 7$  nm highly uniform and monodisperse Yb/Tm: $\text{BaF}_2@\text{Nd}:\text{SrF}_2$  core@shell nanocubes. In this architecture, the  $\text{SrF}_2$  shell not only benefits the enhancement of the near-infrared to near-infrared UC luminescence of the Yb/Tm: $\text{BaF}_2$  core, but also acts as the host to realize the near-infrared to near-infrared down-conversion luminescence of  $\text{Nd}^{3+}$  dopants.

On the other hand, it is interestingly found that, by doping appropriate amount of alkaline-earth ions  $\text{M}^{2+}$  ( $\text{M} = \text{Ca}, \text{Sr}, \text{Ba}$ ; 20 mol%) into  $\text{LnF}_3$ , the hexagonal  $\text{LnF}_3$  ( $\text{Ln} = \text{La}, \text{Ce}, \text{Pr}$ ) NCs are completely transformed into the cubic  $\text{Ln}_{0.8}\text{M}_{0.2}\text{F}_{2.8}$  solid solutions in the solvothermal system (Fig. 9).<sup>38</sup> During the reaction,  $\text{Ln}^{3+}$  react with  $\text{F}^-$  to form the oleic acid capped  $\text{LnF}_3$  crystalline nuclei, which then grow up to NCs with uniform size guided by the long alkyl chains. When adding high content (such as 20 mol%) of  $\text{M}^{2+}$  into the system to replace  $\text{Ln}^{3+}$ , a large amount of vacancies are produced in the  $\text{LnF}_3$  nuclei for charge balance, which break the structural stability of the nuclei, and eventually induce their lattice mutation from hexagonal to cubic. Importantly, phase transition from hexagonal to cubic does not induce obvious size variation but results in a much intensified UC emission (e.g., about 15 times for the  $\text{Tm}^{3+}$

emission), as shown in Fig. 10. This dopant-induced UC enhancement is probably owing to the interplay of the Yb/Er(Tm) activators in the different active sites of the cubic phase, similar to the case in the well-studied  $\text{Ln}^{3+}$ -doped  $\beta\text{-NaYF}_4$ .<sup>57,58</sup>

In a further work, we reported  $\text{Ti}^{4+}$  dopant-induced  $\text{NaYF}_4$  phase transition from cubic-to-hexagonal ( $\alpha \rightarrow \beta$ ) at low temperature (down to  $130^\circ\text{C}$ ) in a liquid–solid–solution (LSS) reaction system.<sup>39</sup> Without  $\text{Ti}^{4+}$  doping,  $\beta\text{-NaYF}_4$  cannot be obtained even when the temperature increases to  $230^\circ\text{C}$ . However, when  $\text{Ti}^{4+}$  ions are introduced into the reaction system, the situation is dramatically altered. With increasing of  $\text{Ti}^{4+}$

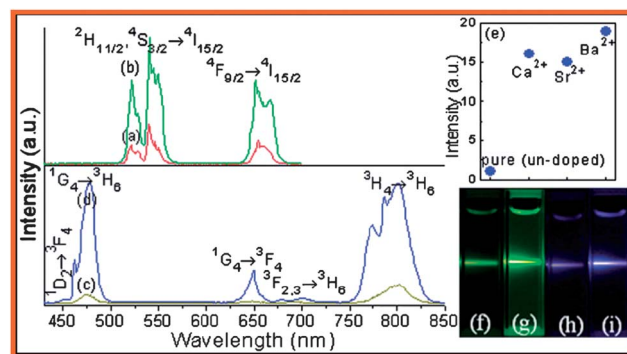


**Fig. 10** UC emission spectra of (a) Yb/Er (10/1 mol%): $\text{LaF}_3$ , (b) Sr/Yb/Er (20/10/1 mol%): $\text{LaF}_3$ , (c) Yb/Tm (10/1 mol%): $\text{LaF}_3$ , and (d) Sr/Yb/Tm (20/10/1 mol%): $\text{LaF}_3$  NCs under 975 nm excitation. (e) Dependence of integrated blue UC intensity of  $\text{Tm}^{3+}$  on the doping ions (20 mol%  $\text{Ca}^{2+}$ ,  $\text{Sr}^{2+}$  and  $\text{Ba}^{2+}$ ); (f)–(i) are the corresponding luminescence photos of samples (a)–(d). Reproduced with permission from ref. 38. © 2011 Royal Society of Chemistry.

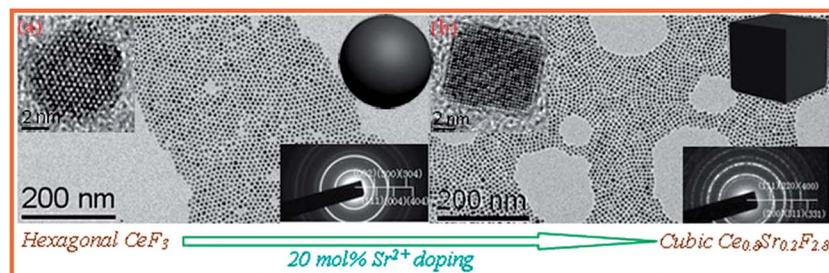


**Fig. 9** TEM micrographs of (a) pure (un-doped) and (b) 20 mol%  $\text{Sr}^{2+}$  doped  $\text{CeF}_3$  samples; insets are the respective HRTEM images and SAED patterns. Reproduced with permission from ref. 38. © 2011 Royal Society of Chemistry.



content the product transforms from the cubic phase to the hexagonal one, and as the  $\text{Ti}^{4+}$  content reaches 10–20 mol% pure  $\beta\text{-NaYF}_4$  is easily achieved at 130 °C (Fig. 11a–d). The doped  $\text{Ti}^{4+}$  ions do not incorporate into the  $\alpha\text{-NaYF}_4$  lattice (by substituting  $\text{Y}^{3+}$ ), but locate on the surfaces of  $\text{NaYF}_4$  owing to the large ionic radii difference between  $\text{Y}^{3+}$  (0.104 nm) and  $\text{Ti}^{4+}$  (0.075 nm) as well as their different charges. The possible mechanism of the  $\text{Ti}^{4+}$  doping-induced  $\alpha \rightarrow \beta$  phase transition of  $\text{NaYF}_4$  is illustrated schematically in Fig. 11e. In the LSS solvothermal system, two phases, *i.e.*, the oleic phase consisting of oleic acid, ethanol, sodium oleate and yttrium oleate, and the aqueous phase containing water, ethanol and  $\text{F}^-$  ions, are formed. At a definite temperature,  $\text{Y}^{3+}$  reacts with  $\text{Na}^+$  and  $\text{F}^-$  to form the  $\alpha\text{-NaYF}_4$  nuclei at the interfaces between the oleic and aqueous phases. Along with the reaction, the *in situ* generated oleic acid molecules adsorb on the surface of the  $\text{NaYF}_4$  nuclei, which results in the staying of these oleophilic nuclei in the oleic phase monodispersedly. With further prolonging the reaction, these nuclei grow up and precipitate from the solution at the bottom of the autoclave. In the case of adding  $\text{Ti}^{4+}$  ions into the system, the reaction process is greatly different. The titanium oleate molecules are formed in the oleic phase, which are easily linked to the surface of the  $\alpha\text{-NaYF}_4$  nuclei. Due to the high hydrolyzation (*i.e.*,

high hydrophilicity) of  $\text{Ti}^{4+}$ , large amount of crystalline nuclei tend to locate at the interfaces between oleic and aqueous phases, which enables them to agglomerate and then grow up. Beyond a certain size, these grown up  $\alpha\text{-NaYF}_4$  NCs are thermodynamically unstable and transform inevitably to the hexagonal phase.<sup>59,60</sup> Remarkably, the key role of the doped  $\text{Ti}^{4+}$  ions is to act as the agglomerators for the cubic  $\text{NaYF}_4$  to accelerate phase transition at low temperature.

Recently, it was demonstrated that  $\text{Mn}^{2+}$ -doping also influences the  $\text{NaYF}_4$  growth dynamics to give simultaneous control of crystalline phase and size of the resulting NCs.<sup>40</sup> Without adding the  $\text{Mn}^{2+}$  ions, the product can be ascribed to a mixture of the cubic and hexagonal phases of  $\text{NaYF}_4$ . Introducing appropriate amount of  $\text{Mn}^{2+}$  ions ( $r = 0.81 \text{ \AA}$ ) with a smaller size than  $\text{Y}^{3+}$  ( $r = 0.89 \text{ \AA}$ ) into  $\text{NaYF}_4$  host dominates the formation of pure cubic-phase  $\text{NaYF}_4$  NCs (Fig. 12a–c). Notably, the  $\text{Mn}^{2+}$ -doping largely inhibited the formation of hexagonal phase at the beginning of the reaction and the dopant-induced hexagonal-to-cubic phase transformation could be achieved after being heated at 200 °C for only 1 hour. Meanwhile, substitution of  $\text{Y}^{3+}$  by  $\text{Mn}^{2+}$  in  $\text{NaYF}_4$  could cause an extra  $\text{F}^-$  ion on the grain surface and then induce transient electric dipoles with their negative poles pointing outward, which substantially hinder the

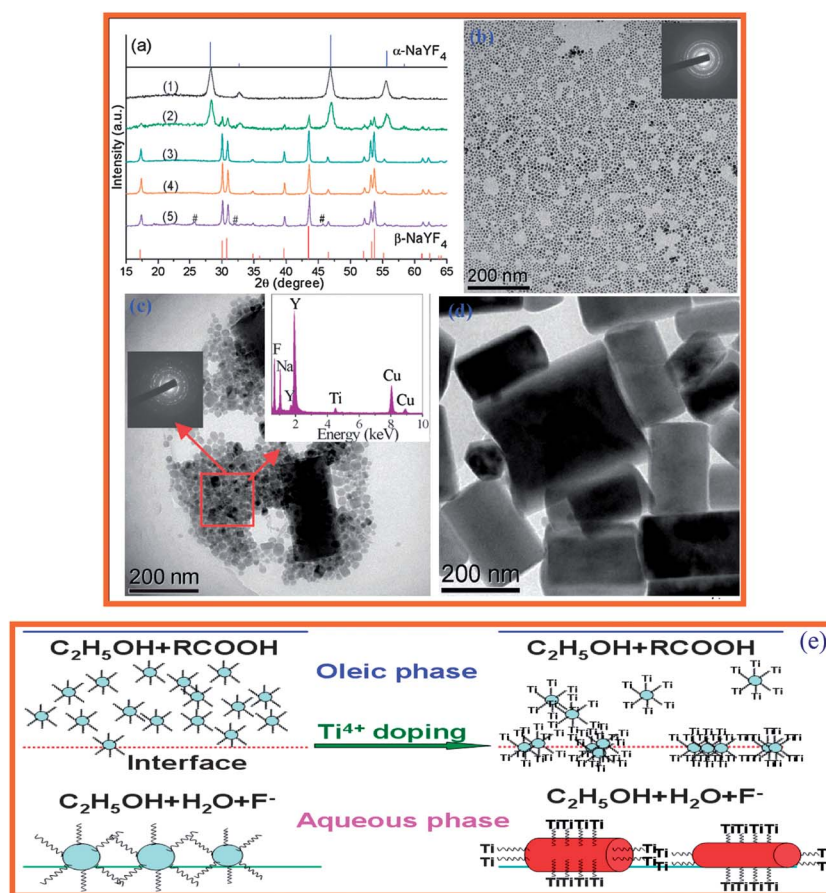


**Fig. 11** (a) XRD patterns of  $\text{NaYF}_4$  doped with various contents of  $\text{Ti}^{4+}$  ( $x$  mol%): (1)  $x = 0$ , (2)  $x = 5$ , (3)  $x = 10$ , (4)  $x = 20$ , and (5)  $x = 30$ ; # represents anatase  $\text{TiO}_2$  phase. TEM micrographs of (b)  $\text{Ti}^{4+}$ -free, (c) 5 mol%  $\text{Ti}^{4+}$ , and (d) 10 mol%  $\text{Ti}^{4+}$  doped  $\text{NaYF}_4$  samples; insets of (b) and (c) are the corresponding SAED patterns of  $\alpha\text{-NaYF}_4$  NCs; EDS spectrum taken from  $\alpha\text{-NaYF}_4$  NCs marked by a square is also provided in the inset of (c). (e) Schematically illustrating the related mechanism for  $\text{Ti}^{4+}$  doping-induced  $\alpha \rightarrow \beta$  phase transition of  $\text{NaYF}_4$ . Reproduced with permission from ref. 39. © 2011 Royal Society of Chemistry.

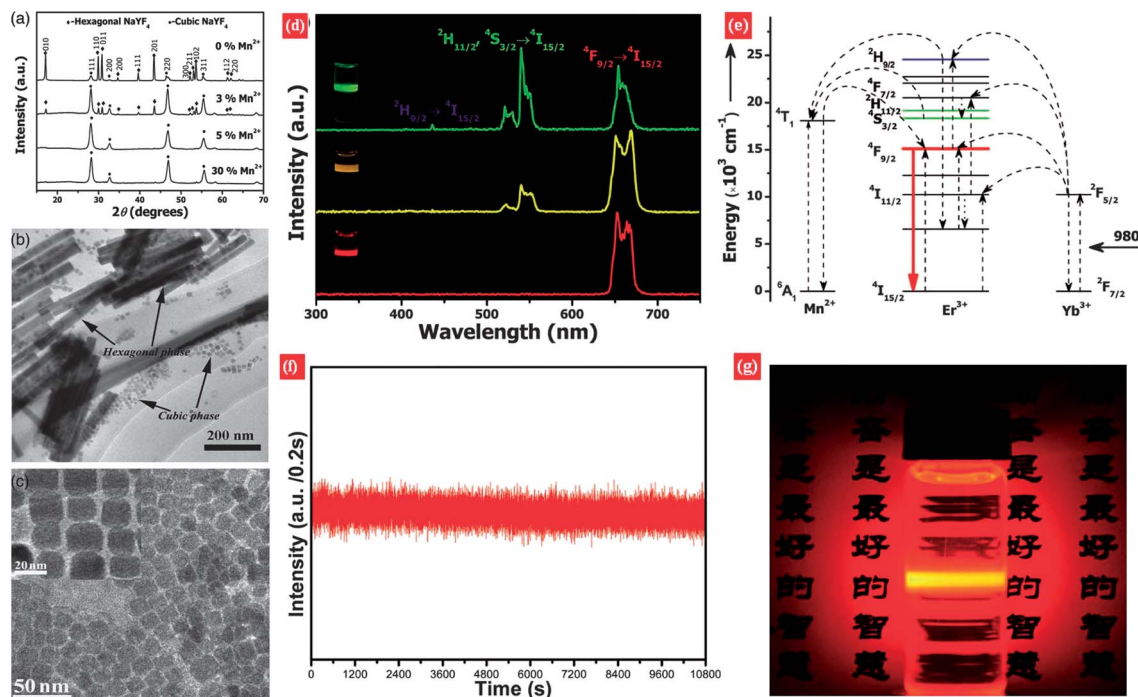


**Fig. 12** (a) XRD patterns of NaYF<sub>4</sub> doped with 0, 3, 5 and 30 mol% Mn<sup>2+</sup> ions. TEM micrographs of NaYF<sub>4</sub> NCs (b) without Mn<sup>2+</sup> dopants and (c) doped with 30 mol% Mn<sup>2+</sup> ions, respectively. (d) UC emission spectra of Yb/Er (18/2 mol%):NaYF<sub>4</sub> NCs doped with 0, 5 and 30 mol% Mn<sup>2+</sup> ions; insets are luminescent photographs of the corresponding samples. (e) Schematic energy level diagram showing the possible UC mechanism of Mn<sup>2+</sup>-doped Yb/Er:NaYF<sub>4</sub> NCs. (f) Luminescence time traces of the 30 mol% Mn<sup>2+</sup>-doped Yb/Er:NaYF<sub>4</sub> NCs acquired with 200 ms time bins under continuous 980 nm laser illumination for more than 3 h, suggesting the durable photostability of the UC NCs. (g) Luminescent photograph of 30 mol% Mn<sup>2+</sup>-doped UC NCs dispersed in hexane. Reproduced with permission from ref. 40. © 2012 Wiley-VCH.

diffusion of F<sup>−</sup> ions needed for crystal growth from the solution to the grain surface due to the charge repulsion, consequently resulting in retardation of the NaYF<sub>4</sub> NC growth. In addition, the doping of Mn<sup>2+</sup> ions into the Yb/Er:NaYF<sub>4</sub> NCs disturbs the transition possibilities between green and red emissions of Er<sup>3+</sup> and facilitates the occurrence of red emission, resulting in an emission color output from green to red by rational controlling the Mn<sup>2+</sup>-doping content, as exhibited in Fig. 12d–g.

#### 4.2 Doping of hetero-valence ions into oxide NCs

Yan *et al.* have demonstrated that doping with Na<sup>+</sup> ions (20 mol %) could lead to the fabrication of monodisperse sub-2 nm-thick Ln<sub>2</sub>O<sub>2</sub>S nanoplates with tunable self-assembly patterns (Fig. 13a–f) and robust fluorescence.<sup>41</sup> The relatively high doping content of Na<sup>+</sup> in the La<sub>2</sub>O<sub>2</sub>S lattice suggests that the growth mechanism of the nanoplates should be governed by the trapped-dopant model.<sup>61,62</sup> Once doped in the La<sub>2</sub>O<sub>2</sub>S host, the Na<sup>+</sup> ions would occupy the La<sup>3+</sup> sites, forming Na<sub>La</sub><sup>xx</sup> defects since the ionic radius of Na<sup>+</sup> (1.02 Å) is very close to that of La<sup>3+</sup> (1.03 Å). After formation of Na<sub>La</sub><sup>xx</sup>, two possible anion vacancies V<sub>O</sub><sup>••</sup> and V<sub>S</sub><sup>••</sup> could be generated to maintain the charge balance. Based on DFT calculations, V<sub>O</sub><sup>••</sup> is the dominant anion vacancy on doping with Na<sup>+</sup> since the formation energy of V<sub>O</sub><sup>••</sup> is always smaller than that of V<sub>S</sub><sup>••</sup> (Fig. 13g). The doping-induced composition control can be further elucidated by the calculated phase diagram after Na<sup>+</sup> doping. Since La<sub>2</sub>S<sub>3</sub> NCs have not been produced in the solution,

and the affinity between La and O is higher than that between La and S, formation of La<sub>2</sub>O<sub>2</sub>S is mainly competitive with formation of La<sub>2</sub>O<sub>3</sub>, and the La<sub>2</sub>S<sub>3</sub> phase is also shown in the diagram only as a constraint for the stable area of La<sub>2</sub>O<sub>2</sub>S. The calculated composition diagram with respect to chemical potential of O (μ<sub>O</sub>) and S (μ<sub>S</sub>) demonstrates the relationship between La<sub>2</sub>O<sub>2</sub>S and La<sub>2</sub>O<sub>3</sub>; doping with Na<sup>+</sup> can greatly increase the stable area of La<sub>2</sub>O<sub>2</sub>S, so that the formation of La<sub>2</sub>O<sub>2</sub>S can tolerate lower μ<sub>S</sub> and higher μ<sub>O</sub> (Fig. 13h). Therefore, it can be concluded that, when Na<sup>+</sup> ions are doped in the NCs, they reduce the amount of O<sup>2−</sup> in the crystals to a certain extent, so that formation of La<sub>2</sub>O<sub>2</sub>S is preferable. This combined theoretical and experimental method can provide new insights into the solution chemistry of NC synthesis, and the present doping strategy of composition control at the nanoscale may also be applicable to the syntheses of many other doped inorganic NCs with unique material properties.

Quasi-spherical monoclinic VO<sub>2</sub> NCs with uniform size and high crystallinity are ideal functional materials for applications in field-effect transistors, smart window coatings and switches. However, the synthesis of quasi-spherical VO<sub>2</sub> NCs has long been a challenge because it requires the induced growth of low-energy surfaces or the suppressed growth of energetically unfavorable high-index faces. Wang *et al.* recently presented a novel doping strategy for the simultaneous control of the size, morphology and poly-morphology of VO<sub>2</sub> NCs ref. 42. Doping can induce the change in crystal structure and exhibits a significant promoting effect on the formation of doped monoclinic VO<sub>2</sub> (M). Specifically,

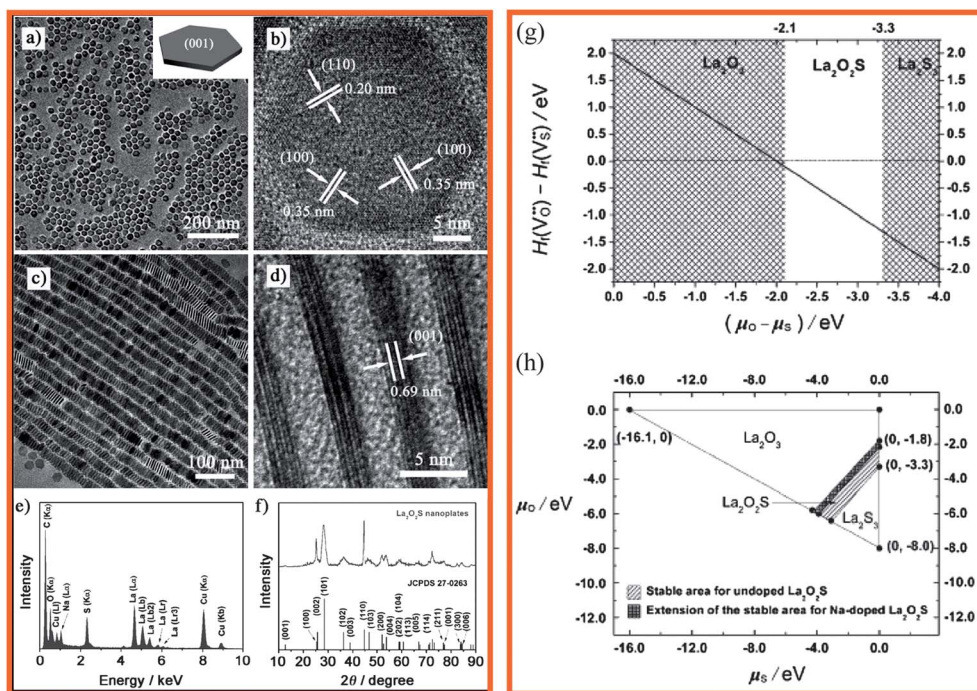


**Fig. 13** (a) TEM and (b) HRTEM (taken with [001] incidence) images of Na-doped La<sub>2</sub>O<sub>2</sub>S nanoplates. (c) TEM and (d) HRTEM (taken with [100] incidence) images of the nanoplate superlattice. (e) EDS spectrum of the nanoplates. (f) Wide-angle XRD pattern of the nanoplates. (g) Calculated difference in vacancy-formation energy versus difference in chemical potential. (h) Calculated phase diagram for un-doped and doped compounds with respect to chemical potential of O and S. Reproduced with permission from ref. 41. © 2011 Wiley-VCH.

doping an appropriate amount of antimony (Sb<sup>3+</sup>) can not only promote the phase transition from tetragonal VO<sub>2</sub> (A) to VO<sub>2</sub> (M), but also decrease the obtained particle size (Fig. 14a–f). Sb<sup>3+</sup> dopants, which are larger in radius and lower in valence than V<sup>4+</sup> ions, can introduce extra oxygen vacancies during the nucleation and growth of VO<sub>2</sub>. These positively charged nuclei may suppress the adsorption of VO<sub>2</sub><sup>2+</sup> aqua ions, and therefore inhibit the growth of the VO<sub>2</sub> (M) nanoparticles (Fig. 14g). Comparably, Sb<sup>5+</sup> dopants that possess higher valence counts than V<sup>4+</sup> ions can induce the growth of VO<sub>2</sub> (M) particles to 200–300 nm width and above 500 nm length. The Sb<sup>3+</sup>-doped VO<sub>2</sub> (M) nanoparticles exhibit excellent properties in metal–semiconductor transformation at transition temperatures, and films obtained by casting these NCs show better optical properties (both visible transmittance and infrared regulation) than those prepared from gas phases, such as sputtering.

Among inorganic nanoparticles, multifunctional cerium oxide (CeO<sub>2</sub>) NCs have garnered considerable attention due to their diverse potential uses in conversion catalysts, three-way catalysts, fuel cells, solar cells, and metal-oxide semiconductor devices. CeO<sub>2</sub> NCs can also be used as therapeutic agents for treatment of cancer and as clinical contrast agents for imaging. Different sized or shaped CeO<sub>2</sub> have different surface area to volume ratios that are important for their catalyzing capability, oxygen-storage capability, and body clearance capability. Despite recent progress in synthesizing CeO<sub>2</sub> NCs, it is still a great challenge to develop a simple method to easily tune their size and shape. Chen *et al.* have demonstrated a facile route to control the size and shape of colloidal CeO<sub>2</sub> NCs through Yb<sup>3+</sup> doping.<sup>43</sup> The average NC size can be easily tuned from 4 to 67

nm by simply increasing the content of Yb<sup>3+</sup> dopants. In addition, pure CeO<sub>2</sub> nanoparticles of spherical shape are converted into nanocubes when the dopant content is higher than 7 mol%. Both the increase in size and the change in shape are ascribed to the increase in the growth rate of NCs due to the cationic doping with a lower valence. After Yb<sup>3+</sup> ions are introduced into the system, they occupy Ce<sup>4+</sup> sites and generate negative charges at the center of NCs due to the lower valence of Yb<sup>3+</sup> than Ce<sup>4+</sup>. In order to establish charge balance, extra positive ions have to be introduced into the grain surface, which form transient electric dipoles with the direction pointing from the center to the surface of NCs. These electric dipoles will exercise a pulling force and attract OH<sup>−</sup> ions to grain surface, thus promoting CeO<sub>2</sub> growth (Fig. 15). As more dopants are introduced, more such electric dipoles are generated, and subsequently a larger sized CeO<sub>2</sub> NCs are achieved due to the quicker growth rate.

Cu<sub>2</sub>O has drawn attention recently for its potential applications in catalyst and solar cells. Tang *et al.* demonstrated that the introduction of Zn<sup>2+</sup> dopants was critical to the dramatic shape evolution of Cu<sub>2</sub>O microcrystals (Fig. 16).<sup>44</sup> Zn<sup>2+</sup>-doped Cu<sub>2</sub>O crystals with well-defined shapes, from 50-facet and 26-facet to 8-facet were realized for the first time. Reaction mechanism studies showed that the relative content of Zn(NO<sub>3</sub>)<sub>2</sub> in the reagents was a key factor which caused a lower content of Cu(OH)<sub>4</sub><sup>2−</sup> as well as a lower oriented growth rate, and eventually led to fewer plane numbers in the doped microcrystals. Interestingly, the Zn<sup>2+</sup>-doped Cu<sub>2</sub>O crystals showed the p-type semiconductor characteristics although the pure (un-doped) Cu<sub>2</sub>O ones exhibited the n-type feature.



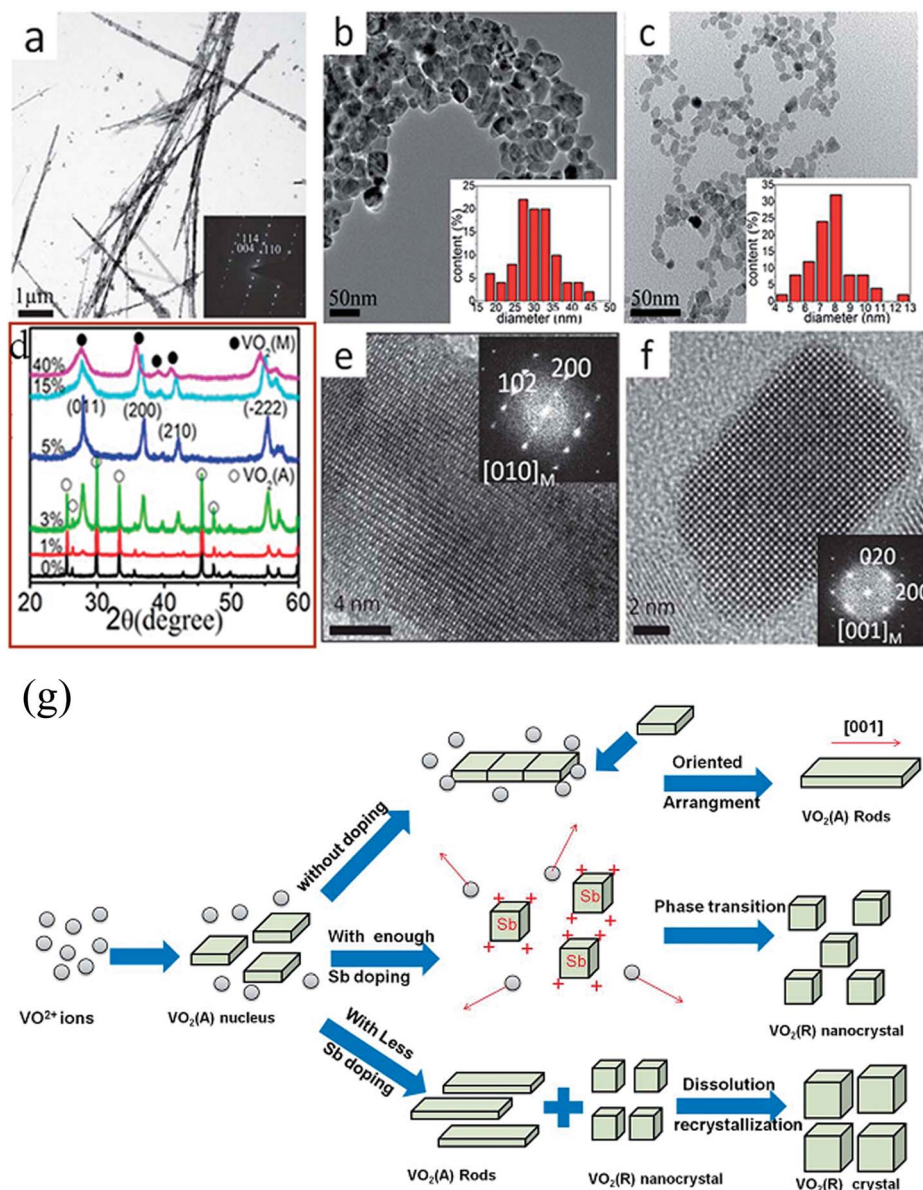


**Fig. 14** TEM micrographs of the  $\text{VO}_2$  NCs doped with different content of  $\text{Sb}^{3+}$ : (a) 1%, (b) 3%, and (c) 40%. (d) XRD patterns of the  $\text{VO}_2$  NCs with and without  $\text{Sb}^{3+}$  doping. HRTEM images (inset, the SAED pattern) of the  $\text{VO}_2$  NCs with a  $\text{Sb}^{3+}$  addition of (e) 3% and (f) 40%. (g) A schematic illustration of the evolution of  $\text{VO}_2$  NCs under the influence of  $\text{Sb}^{3+}$  doping. Reproduced with permission from ref. 42. © 2012 Royal Society of Chemistry.

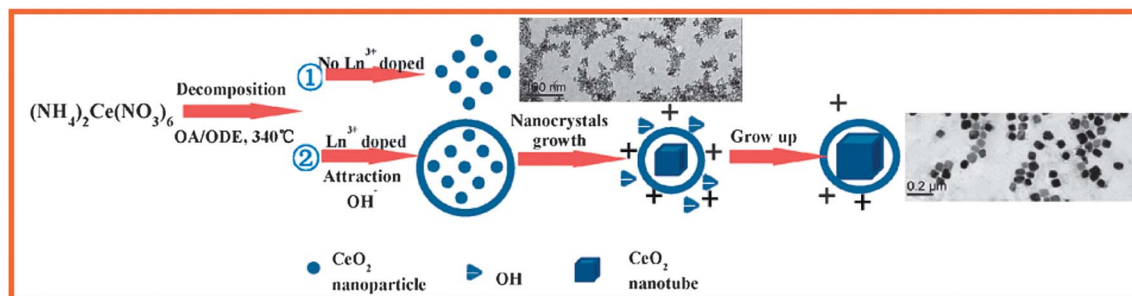


**Fig. 15** Schematic illustration of the impact of  $\text{Ln}^{3+}$  doping on the size and shape of  $\text{CeO}_2$  NCs. Reproduced with permission from ref. 43. © 2011 Royal Society of Chemistry.

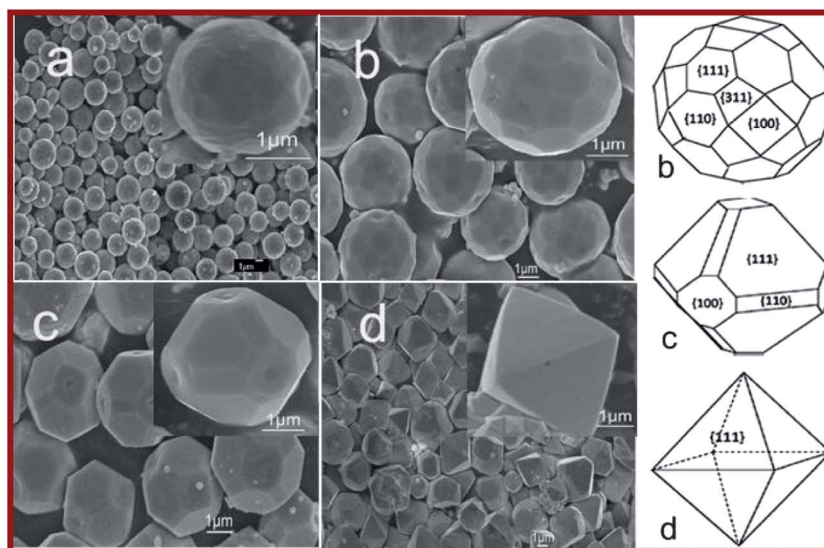


**Fig. 16** SEM images of the  $\text{Cu}_2\text{O}$  products obtained from the reactions with different molar ratios of  $\text{Cu}(\text{OAc})_2$  and  $\text{Zn}(\text{NO}_3)_2$  in the reagent: (a) 4 : 0, (b) 4 : 1, (c) 4 : 2 and (d) 4 : 3. The insets are magnified images of a single crystal. The right side denotes the schematic models of the corresponding products in (b–d). Reproduced with permission from ref. 44. © 2012 American Chemical Society.

Generally speaking, similar to the cases of the homo-valence ion doping, the hetero-valence ions doping into the hosts also have significant impact on the nucleation and growth of many fluoride and oxide nanocrystals, and provide a fundamental route to modify the phase structures, sizes, shapes as well as properties of nanomaterials. Impressively, the microstructure and performance modification of functional nanomaterials by hetero-valence ions doping is more preponderant than that by homo-valence ions doping.

## 5 Control of $\text{Ln}^{3+}$ dopant distribution in core/shell NCs

For lanthanide ( $\text{Ln}^{3+}$ ) doped UC NCs, the doping host and the distribution of doping activators in the host are essential for realizing favorable optical performance, such as a high UC efficiency and a controllable emission profile. However, the distribution of dopants in the host is naturally formed during nucleation and growth of NCs, related to the intrinsic structural characteristics of the host. For example,  $\text{Ln}^{3+}$  dopants are uniformly distributed in  $\text{NaGdF}_4$  because of the similar electronic configurations of  $\text{Ln}^{3+}$  and  $\text{Gd}^{3+}$ , while their distribution is usually inhomogeneous (*i.e.*, forming clusters) in  $\text{CaF}_2$  and  $\text{Na}_3\text{Zr}(\text{Hf})\text{F}_7$  due to the requirement of extra charge compensation for the substitution of  $\text{Ca}^{2+}$  or  $\text{Zr}^{4+}(\text{Hf}^{4+})$  by  $\text{Ln}^{3+}$ .<sup>63–66</sup> As a result, when doping the same content of Yb/Er (20/2 mol%) into  $\text{NaGdF}_4$ ,  $\text{CaF}_2$  and  $\text{Na}_3\text{Zr}(\text{Hf})\text{F}_7$  hosts respectively, quite different UC emission colors are observed: Yb/Er: $\text{NaGdF}_4$  exhibits green color,<sup>67</sup> Yb/Er: $\text{CaF}_2$  yellow one,<sup>68</sup> while Yb/Er: $\text{Na}_3\text{Zr}(\text{Hf})\text{F}_7$  red one.<sup>66</sup> Therefore, controlling dopant distribution in a definite host is of great significance for manipulating UC emission colors, but remains a formidable challenge so far.

Alternatively, controlling the  $\text{Ln}^{3+}$  dopant distribution and subsequently fine-tuning the multicolor UC emissions may be realized by constructing the core/shell nanostructures. As a

proof-of-concept experiment, Chen *et al.* recently proposed a strategy to control  $\text{Ln}^{3+}$  distribution in core/shell NCs, where  $\text{Tm}^{3+}$  and  $\text{Yb}^{3+}$  ions are co-doped in  $\text{NaGdF}_4$  core and  $\text{Eu}^{3+}$  ions are doped in  $\text{NaGdF}_4$  shell NCs.<sup>69</sup> By designing such core/shell nanostructures and the double sensitizations from both  $\text{Yb}^{3+}$  and  $\text{Tm}^{3+}$ , eye-visible UC luminescence resulting from  $\text{Eu}^{3+}$  can be clearly detected. Such remarkable UC luminescence of  $\text{Eu}^{3+}$  in core/shell NCs was found to be about one order of magnitude higher than the triply doped core-only counterparts, which is mainly due to the effective elimination of the deleterious cross-relaxations between doped  $\text{Eu}^{3+}$ ,  $\text{Yb}^{3+}$  and  $\text{Tm}^{3+}$  ions through controlling their distribution in the core and shell respectively. Notably, this is the first example for the realization intense UC emission of  $\text{Ln}^{3+}$  ions beyond the  $\text{Er}^{3+}$ ,  $\text{Tm}^{3+}$ , and  $\text{Ho}^{3+}$  ones.

Later on, this  $\text{Ln}^{3+}$ -dopant controlling strategy was refined and then extended to realize intense UC emissions for a series of  $\text{Ln}^{3+}$  activators in the Yb/Tm: $\text{NaGdF}_4$ @Ln: $\text{NaGdF}_4$  (Ln = Tb, Eu, Dy and Sm) core@shell NCs by Liu and co-workers.<sup>70</sup> By rational design of the core@shell structure with a set of  $\text{Ln}^{3+}$  dopants incorporated into separated layers at precisely defined concentrations, efficient UC emission can be realized through gadolinium sublattice-mediated energy migration (defined as energy migration-mediated UC which was never observed before) for a wide range of  $\text{Ln}^{3+}$  activators without long-lived intermediary energy states (Fig. 17a–h). Similarly, the use of the core@shell structure allows the elimination of deleterious cross-relaxation between  $\text{Ln}^{3+}$  ions. This effect enables fine-tuning of UC emission through trapping of the migrating energy by the activators. Furthermore, to prevent surface quenching of excitation energy, an optically inert  $\text{NaYF}_4$  layer was epitaxially grown around the core@shell NCs.<sup>71</sup> With the help of such active-core@active-shell@inert-shell architecture, the energy migrates over Gd sublattices and is adequately trapped by the activator ions embedded in host lattices (Fig. 17i). Importantly, the  $\text{NaYF}_4$  shell-coating strategy gives

access to tunable UC emissions from a variety of activators ( $\text{Dy}^{3+}$ ,  $\text{Sm}^{3+}$ ,  $\text{Tb}^{3+}$ , and  $\text{Eu}^{3+}$ ) doped at very low concentrations (down to 1 mol%), as exhibited in Fig. 17j. Indeed, these findings suggest a general approach to constructing a new class of luminescent materials with tunable UC emissions by controlling the distribution of  $\text{Ln}^{3+}$  dopants and the manipulation of energy transfer within a nanoscopic region.

In fact, the strategy of controlling  $\text{Ln}^{3+}$  dopant distribution in core@shell NCs can also be used to enhance UC emission of dopants in core. Capobianco and co-workers have synthesized Yb/Er (20/2 mol%)  $\text{NaGdF}_4$  active-core/Yb (20 mol%): $\text{NaGdF}_4$  active-shell NCs and have demonstrated a significant increase in UC intensity compared to Yb/Er (20/2 mol%): $\text{NaGdF}_4$  active-core/ $\text{NaGdF}_4$  inert-shell and Yb/Er (20/2 mol%): $\text{NaGdF}_4$  core-only nanoparticles (Fig. 18).<sup>72</sup> The active-shell serves two purposes: (i) to protect the luminescent  $\text{Er}^{3+}$  activators from the

non-radiative decay and (ii) to transfer NIR absorbed radiation to the luminescent core. As a comparison, they synthesized Yb/Er (40/2 mol%): $\text{NaGdF}_4$  core-only with the same total  $\text{Yb}^{3+}$  content as the active-core/active-shell nanoparticles. In this case, the UC intensity in the 40%  $\text{Yb}^{3+}$ -doped NCs is significantly weaker than that of the active-core/active-shell and even weaker than that of the Yb/Er (20/2 mol%): $\text{NaGdF}_4$  core-only nanoparticles. The enhancement of UC emission was believed to be caused by energy transfer of excited  $\text{Yb}^{3+}$  ions in the active-shell to the dopant ions in the active-core, which are spatially separated thereby limiting the efficiency of concentration quenching such as that observed in Yb/Er (40/2 mol%): $\text{NaGdF}_4$  core-only NCs. Similarly, Lin *et al.* have achieved about several hundred-time UC enhancement of Yb/Er: $\text{BaGdF}_5$  core NCs through coating Yb: $\text{BaGdF}_5$  shell on the surface of core.<sup>73</sup>

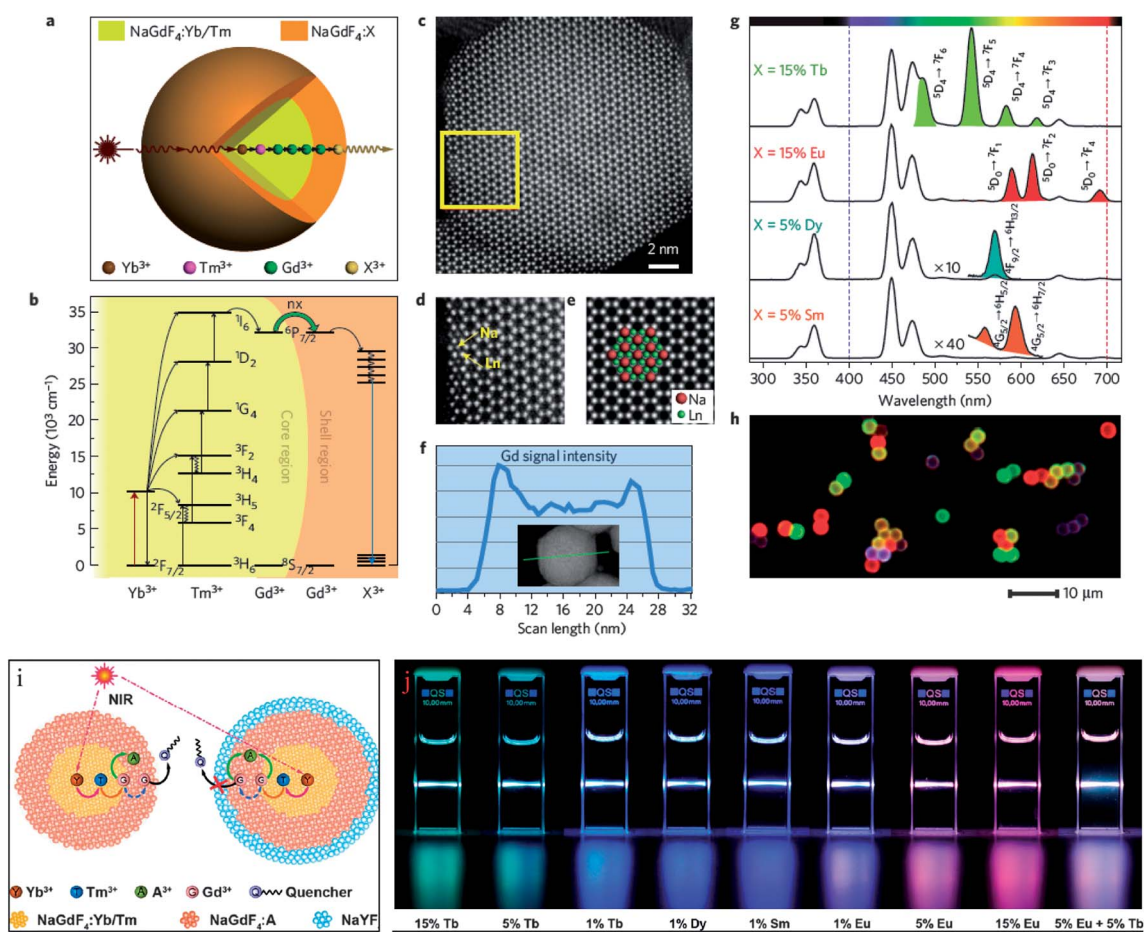


**Fig. 17** (a) Schematic design of a  $\text{Ln}^{3+}$ -doped Yb/Tm: $\text{NaGdF}_4$ @X: $\text{NaGdF}_4$  core@shell NC for UC emissions (X: activator ion). (b) Proposed energy transfer mechanisms in the core@shell NCs. (c) High-resolution STEM image taken at [001] incidence of an individual NC comprising a Yb/Tm (49/1%): $\text{NaGdF}_4$  core and a Tb (15%): $\text{NaGdF}_4$  shell, revealing the single-crystalline nature of the crystal. (d) An enlarged view of the selected area in (c), indicated by a yellow box, showing lanthanide (Ln) and Na atomic columns. (e) Digitally processed STEM image by imposing projection symmetry to enhance the signal-to-noise ratio. (f) EELS line scan conducted with STEM imaging (inset) on a Yb/Tm: $\text{NaGdF}_4$ @Tb: $\text{NaGdF}_4$  nanoparticle, indicating a higher Gd concentration in the peripheral region of the crystal that is very consistent with the designed core@shell structure. (g) Emission spectra of the as-prepared Yb/Tm: $\text{NaGdF}_4$ @X: $\text{NaGdF}_4$  core@shell NCs doped with different activators (activator emissions are highlighted with color). (h) Luminescent micrograph of polystyrene beads tagged with core@shell NCs of Yb/Tm: $\text{NaGdF}_4$ @ $\text{NaGdF}_4$  (blue), Yb/Tm: $\text{NaGdF}_4$ @Tb: $\text{NaGdF}_4$  (green), Yb/Tm: $\text{NaGdF}_4$ @Eu: $\text{NaGdF}_4$  (red), and a binary mixture of Yb/Tm: $\text{NaGdF}_4$ @Tb: $\text{NaGdF}_4$  and Yb/Tm: $\text{NaGdF}_4$ @Eu: $\text{NaGdF}_4$  (yellow), respectively. (i) Schematic illustration of the energy transfer mechanism in the core@shell and  $\text{NaYF}_4$ -coated core@shell@shell NCs. (j) Tunable multi-color UC emissions in the representative Yb/Tm: $\text{NaGdF}_4$ @X: $\text{NaGdF}_4$ @ $\text{NaYF}_4$  samples in cyclohexane solution ( $2 \text{ mg mL}^{-1}$ ) under irradiation of a 980 nm laser. Reproduced with permission from ref. 70 and 71. © 2011 Nature Publishing Group. © 2013 American Chemical Society.



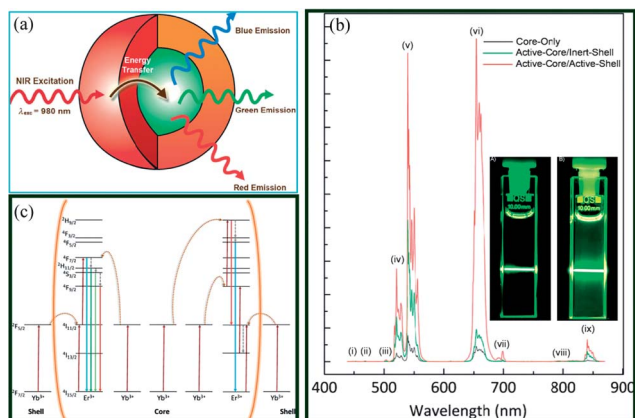


**Fig. 18** (a) General depiction of the active-core/active-shell architecture showing the absorption of NIR light by the Yb-rich shell (represented in red) and subsequent energy transfer to the Yb/Er co-doped core (represented in green), leading to upconverted blue, green, and red emissions. (b) UC emission spectra of colloidal Yb/Er:NaGdF<sub>4</sub> (core-only), Yb/Er:NaGdF<sub>4</sub>@NaGdF<sub>4</sub> (active-core/inert-shell) and Yb/Er:NaGdF<sub>4</sub>@Yb:NaGdF<sub>4</sub> (active-core/active-shell) NCs in toluene (1 wt%) following excitation with 980 nm radiation; insets are the corresponding luminescent photos of Yb/Er:NaGdF<sub>4</sub>@NaGdF<sub>4</sub> and Yb/Er:NaGdF<sub>4</sub>@Yb:NaGdF<sub>4</sub> NCs respectively. (c) The proposed UC mechanisms in active-core@active-shell NCs. Reproduced with permission from ref. 72. © 2009 Wiley-VCH.

We recently realized the dual-modal emissions of Ln<sup>3+</sup> by cutting the adverse energy transfer between Ln<sup>3+</sup> ions separated in the core and shell respectively. For instance, we achieved the dual-modal NIR-to-NIR UC and downconversion (DC) emissions in the Yb/Tm:BaF<sub>2</sub>@Nd:SrF<sub>2</sub> active-core/active-shell nanocubes.<sup>37</sup> Remarkably, both UC and DC emission intensities of the active-core/active-shell nanocubes are about one order of magnitude higher than those of the triply doped Yb/Tm:Nd:BaF<sub>2</sub>/SrF<sub>2</sub> active-core/inert-shell counterparts, due to the inhibition of the

deleterious energy transfer from Tm<sup>3+</sup> to Nd<sup>3+</sup> as well as from Nd<sup>3+</sup> to Yb<sup>3+</sup> in the active-core/active-shell NCs that are reasonably separated in space (Yb<sup>3+</sup>/Tm<sup>3+</sup> residing in core while Nd<sup>3+</sup> in shell). Another example is that we have successfully fabricated monodisperse and uniform Er:NaGdF<sub>4</sub>@Ho:NaGdF<sub>4</sub>@NaGdF<sub>4</sub> NCs, where the intermediate shell not only plays a passivation role to enhance the UC luminescence of Er<sup>3+</sup> in the core, but also acts as the host to realize the UC luminescence of Ho<sup>3+</sup>.<sup>74</sup> Importantly, doping of Er<sup>3+</sup> and Ho<sup>3+</sup> into core and shell respectively breaks effectively the adverse energy transfers between Er<sup>3+</sup> and Ho<sup>3+</sup>, resulting in the intense UC emissions from both Er<sup>3+</sup> and Ho<sup>3+</sup> dopants simultaneously (Fig. 19). These novel core/shell NCs, which can be excited by ultra-broadband NIR photons transparent to c-Si and emit visible-NIR ones above the c-Si bandgap, may find potential application in c-Si solar cells to enhance the energy efficiency.

## 6 Conclusions and perspectives

In this review article, an overview of the recently developed impurity-doping synthesis strategy for functional nanomaterials is presented. Impurity doping has been demonstrated to have significant impact on nucleation and growth of many fluoride and oxide nanocrystals, which provides a fundamental route to modify the phase structures, sizes, shapes as well as properties of nanocrystals. Several mechanisms, such as doping-induced alteration of surface charge density, doping-induced generation of transient electric dipoles, doping-induced decrease of phase-transition energy barrier, and doping-induced instability of phase structure *etc.*, were proposed to explain the various experimental phenomena. In stark contrast to the conventional synthetic techniques that require stringent control over several experimental variables, the impurity-doping approach requires

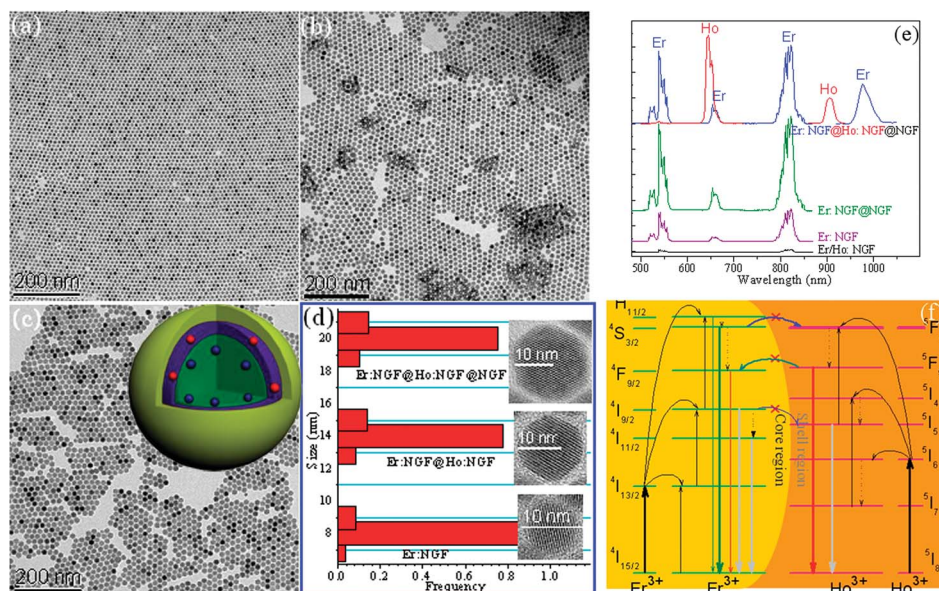


**Fig. 19** TEM micrographs of (a) Er:NaGdF<sub>4</sub>, (b) Er:NaGdF<sub>4</sub>@Ho:NaGdF<sub>4</sub> and (c) Er:NaGdF<sub>4</sub>@Ho:NaGdF<sub>4</sub>@NaGdF<sub>4</sub> core@shell NCs; (d) histograms showing nanoparticle size distribution for these three samples; inset is HRTEM image of individual grain in the corresponding sample. (e) UC emission spectra of core and core@shell NCs. (f) Energy levels of Er<sup>3+</sup> and Ho<sup>3+</sup> ions, showing possible energy transfer UC processes in the Er:NaGdF<sub>4</sub>@Ho:NaGdF<sub>4</sub> core@shell NCs where the adverse Er<sup>3+</sup> ↔ Ho<sup>3+</sup> energy transfers are effectively avoided. Reproduced with permission from ref. 74. ©i 2012 Royal Society of Chemistry.

modification of only a single variable (dopant concentration), for tuning the microstructure and performance of nanocrystals.

For upconversion nanocrystals mainly concerned, lanthanide dopants act as luminescent activators and the controlling of their distribution in the host is essential for realizing a high quantum yield and a controllable emission profile. Several strategies to control lanthanide distribution in core@shell architectures are provided. The key point is to separate different functional lanthanide activators into core and shell with precisely defined concentrations respectively, which allows the elimination of deleterious cross-relaxation between them. Subsequently, efficient and unprecedented color-tunable upconversion emissions are realized in several core@shell nanocrystals by controlling the distribution of lanthanide dopants and the manipulation of energy transfer within a nanoscopic region. Despite the fact that some successful results in core@shell NCs were obtained, it is still a major challenge to realize the controlling of lanthanide dopant distribution in a definite host since the distribution of dopants in the host is naturally formed during nucleation and growth of nanocrystals, related to the intrinsic structural characteristics of the host. In addition, the mechanisms of impurity doping-induced upconversion enhancement of nanocrystals are still not clear. Further work should be carried out to understand the relationship between doping-induced structural variation and upconversion property modification. This will help us to choose appropriate doping host and dopants and finally to greatly improve upconversion luminescence of the designed nanocrystals.

Overall, the newly developed impurity-doping strategy has exhibited great potential for controllable syntheses of many technologically important nanomaterials. However, most of the reported experimental results are primitive and the related basic scientific problems are yet to be resolved. In the near future, there are a number of research issues that are particularly interesting, but require concerted effort for success: (1) fabrication of more materials, where impurities with various valence can be easily incorporated in the hosts, is urgently needed to discern the different roles of the impurities with different valence on their microstructure and performance; (2) direct evidences are required to reveal where the doped impurities are actually located in the hosts, and what impacts they impart to the electronic configurations of the nanocrystals; (3) do the impurity dopants play the key role in initial nucleation or growth of nanocrystals, or even in both stages? (4) is it possible to conclude the general or universal mechanisms for understanding the doping-induced microstructure modifications of nanocrystals, enabling the fine designs and controlled syntheses of the functional materials we want. Definitely, the combination of experiments and theoretical studies such as *ab initio* simulations, density functional calculations, diffusion kinetics and phase transformation thermodynamics/kinetics calculations, will provide new insights and help to solve these scientific issues.

## Acknowledgements

This work was supported by National Natural Science Foundation of China (51172231, 21271170, 11204301 and 51202244), Natural Science Foundation of Fujian for Distinguished Young

Scholars (2012J06014), the External Cooperation Program of CAS (GJHZ1133) and Chunmiao Project of Haixi Institute of CAS (CMZX-2013-004).

## References

- 1 X. W. Liu, D. S. Wang and Y. D. Li, *Nano Today*, 2012, **7**, 448.
- 2 S. Linic, P. Christopher and D. B. Ingram, *Nat. Mater.*, 2011, **10**, 911.
- 3 D. Q. Chen, Y. S. Wang and M. C. Hong, *Nano Energy*, 2012, **1**, 73.
- 4 F. Wang and X. G. Liu, *Chem. Soc. Rev.*, 2009, **38**, 976.
- 5 E. Jang, S. Jun, H. Jang, J. Lim, B. Kim and Y. Kim, *Adv. Mater.*, 2010, **22**, 3076.
- 6 X. Wang, J. Zhuang, Q. Peng and Y. D. Li, *Nature*, 2005, **437**, 121.
- 7 Y. C. Zhu, T. Me, Y. Wang and Y. T. Qian, *J. Mater. Chem.*, 2011, **21**, 11457.
- 8 H. X. Mai, Y. W. Zhang, R. Si, Z. G. Yan, L. D. Sun, L. P. You and C. H. Yan, *J. Am. Chem. Soc.*, 2006, **128**, 6426.
- 9 J. C. Boyer, L. A. Cuccia and J. A. Capobianco, *Nano Lett.*, 2007, **7**, 847.
- 10 C. Wang, K. Ryu, L. G. De Arco, A. Badmaev, J. L. Zhang, X. Lin, Y. C. Che and C. W. Zhou, *Nano Res.*, 2010, **3**, 831.
- 11 N. Niu, P. P. yang, F. He, X. Zhang, S. L. Gai, C. X. Li and J. Lin, *J. Mater. Chem.*, 2012, **22**, 10889.
- 12 Y. Tian, B. J. Chen, H. Q. Yu, R. N. Hua, X. P. Li, J. S. Sun, L. H. Cheng, H. Y. Zhong, J. S. Zhang, Y. F. Zheng, T. T. Yu and L. B. Huang, *J. Colloid Interface Sci.*, 2011, **360**, 586.
- 13 D. J. Norris, A. L. Efros and S. C. Erwin, *Science*, 2008, **319**, 1776.
- 14 G. K. Liu and X. Y. Chen, *Frontier Developments in Optics and Spectroscopy*, ed. B. Di Bartolo and O. Forte Boston College, Google Books, 2008, ch. 13, pp. 1–26.
- 15 P. N. Prasad, *Nanophotonics*, Wiley, New York, 2004.
- 16 R. S. Meltzer, S. P. Feofilov, B. Tissue and H. B. Yuan, *Phys. Rev. B: Condens. Matter Mater. Phys.*, 1999, **60**, R14012.
- 17 D. Jia, Y. Wang, X. Guo, K. Li, Y. K. Zou and W. Jia, *J. Electrochem. Soc.*, 2007, **154**, J1.
- 18 L. Q. Liu, E. Ma, R. F. Li, G. K. Liu and X. Y. Chen, *Nanotechnology*, 2007, **18**, 015403.
- 19 L. Yu, H. Song, S. Lu, Z. Liu, L. Yang and X. Kong, *J. Phys. Chem. B*, 2004, **104**, 16697.
- 20 P. A. Tanner, *J. Nanosci. Nanotechnol.*, 2005, **5**, 1455.
- 21 M. N. Luwang, R. S. Ningthoujam, Jagannath, S. K. Srivastava and R. K. Vatsa, *J. Am. Chem. Soc.*, 2010, **132**, 2759.
- 22 Y. P. Du, Y. W. Zhang, Z. G. Yan, L. D. Sun and C. H. Yan, *J. Am. Chem. Soc.*, 2009, **131**, 16364.
- 23 A. Aebischer, M. Hostettler, J. Hauser, K. Krämer, T. Weber, H. U. Güdel and H. B. Bürgi, *Angew. Chem., Int. Ed.*, 2006, **45**, 2802.
- 24 F. Wang, Y. Han, C. S. Lim, Y. H. Lu, J. Wang, J. Xu, H. Y. Chen, C. Zhang, M. H. Hong and X. G. Liu, *Nature*, 2010, **463**, 1061.
- 25 D. Q. Chen, Y. L. Yu, F. Huang, A. P. Yang and Y. S. Wang, *J. Mater. Chem.*, 2011, **21**, 6186.
- 26 Y. Tian, R. N. Hua, B. J. Chen, N. S. Yu, W. Zhang and L. Y. Na, *CrystEngComm*, 2012, **14**, 8110.

- 27 C. F. Xu, M. Ma, L. W. Yang, S. J. Zeng and Q. B. Yang, *J. Colloid Interface Sci.*, 2012, **368**, 49.
- 28 Q. Q. Dou and Y. Zhang, *Langmuir*, 2011, **27**, 13236.
- 29 D. M. Yang, Y. L. Dai, P. A. Ma, X. J. Kang, M. M. Shang, Z. Y. Cheng, C. X. Li and J. Lin, *J. Mater. Chem.*, 2012, **22**, 20618.
- 30 D. Q. Chen, Y. L. Yu, F. Huang, P. Huang, A. P. Yang, Z. X. Wang and Y. S. Wang, *Chem. Commun.*, 2011, **47**, 11083.
- 31 X. D. Feng, D. C. Sayle, Z. L. Wang, M. S. Paras, B. Santora, A. C. Sutorik, T. X. T. Sayle, Y. Yang, Y. Ding, X. D. Wang and Y. S. Her, *Science*, 2006, **312**, 1504.
- 32 Y. Wang, T. J. Hou, S. Tian, S. T. Lee and Y. Y. Li, *J. Phys. Chem. C*, 2011, **115**, 7706.
- 33 L. Wu, T. J. Hou, Y. Wang, Y. F. Zhao, Z. Y. Guo, Y. Y. Li and S. T. Lee, *J. Alloys Compd.*, 2012, **541**, 250.
- 34 Y. F. Yang, Y. Z. Jin, H. P. He, Q. L. Wang, Y. Tu, H. M. Lu and Z. Z. Ye, *J. Am. Chem. Soc.*, 2010, **132**, 13381.
- 35 C. R. De Silva, S. Smith, I. Shim, J. Pyun, T. Gutu, J. Jiao and Z. P. Zheng, *J. Am. Chem. Soc.*, 2009, **131**, 6336.
- 36 D. Q. Chen, Y. L. Yu, F. Huang, P. Huang, A. P. Yang and Y. S. Wang, *J. Am. Chem. Soc.*, 2010, **132**, 9976.
- 37 D. Q. Chen, Y. L. Yu, F. Huang, H. Lin, P. Huang, A. P. Yang, Z. X. Wang and Y. S. Wang, *J. Mater. Chem.*, 2012, **22**, 2632.
- 38 D. Q. Chen, Y. L. Yu, F. Huang and Y. S. Wang, *Chem. Commun.*, 2011, **47**, 2601.
- 39 D. Q. Chen, P. Huang, Y. L. Yu, F. Huang, A. P. Yang and Y. S. Wang, *Chem. Commun.*, 2011, **47**, 5801.
- 40 G. Tian, Z. J. Gu, L. J. Zhou, W. Y. Yin, X. X. Liu, L. Yan, S. Jin, W. L. Ren, G. M. Xing, S. J. Li and Y. L. Zhao, *Adv. Mater.*, 2012, **24**, 1226.
- 41 Y. Ding, J. Gu, J. Ke, Y. W. Zhang and C. H. Yan, *Angew. Chem., Int. Ed.*, 2011, **50**, 12330.
- 42 Y. F. Gao, C. X. Cao, L. Dai, H. J. Luo, M. Kanehira, Y. Ding and Z. L. Wang, *Energy Environ. Sci.*, 2012, **5**, 8708.
- 43 H. L. Qiu, G. Y. Chen, R. W. Fan, C. Cheng, S. W. Hao, D. Y. Chen and C. H. Yang, *Chem. Commun.*, 2011, **47**, 9648.
- 44 B. J. Heng, T. Xiao, W. Tao, X. Y. Hu, X. Q. Chen, B. X. Wang, D. M. Sun and Y. W. Tang, *Cryst. Growth Des.*, 2012, **12**, 3998.
- 45 F. Auzel, *Chem. Rev.*, 2004, **104**, 139.
- 46 M. Haase and H. Schäfer, *Angew. Chem., Int. Ed.*, 2011, **50**, 5808.
- 47 M. Nyk, R. Kumar, T. Y. Ohulchanskyy, E. J. Bergey and P. N. Prasad, *Nano Lett.*, 2008, **8**, 3834.
- 48 R. Kumar, M. Nyk, T. Y. Ohulchanskyy, C. A. Flask and P. N. Prasad, *Adv. Funct. Mater.*, 2009, **19**, 853.
- 49 T. Y. Cao, Y. Yang, Y. Gao, J. Zhou, Z. Q. Li and F. Y. Li, *Biomaterials*, 2011, **32**, 2959.
- 50 Q. Liu, Y. Sun, T. S. Yang, W. Feng, C. G. Li and F. Y. Li, *J. Am. Chem. Soc.*, 2011, **133**, 17122.
- 51 Y. S. Liu, D. T. Tu, H. M. Zhu, E. Ma and X. Y. Chen, *Nanoscale*, 2013, **5**, 1369.
- 52 K. Krämer, D. Biner, G. Frei, H. U. Güdel, M. P. Hehlen and S. R. Lüthi, *Chem. Mater.*, 2004, **16**, 1244.
- 53 A. A. Kaminskii, *Laser Photonics Rev.*, 2007, **1**, 93.
- 54 D. Q. Chen, L. Lei, J. Xu, A. P. Yang and Y. S. Wang, *Nanotechnology*, 2013, **24**, 085708.
- 55 L. R. Batsanova, *Russ. Chem. Rev.*, 1971, **40**, 465.
- 56 B. P. Sobolev, K. B. Seiranian, L. S. Garashina and P. P. Fedorov, *J. Solid State Chem.*, 1979, **28**, 51.
- 57 P. Ptacek, H. Schäfer, K. Kömpe and M. Haase, *Adv. Funct. Mater.*, 2007, **17**, 3843.
- 58 D. T. Tu, Y. S. Liu, H. M. Zhu, R. F. Li, L. Q. Liu and X. Y. Chen, *Angew. Chem., Int. Ed.*, 2013, **52**, 1128.
- 59 G. S. Yi and G. M. Chow, *Adv. Funct. Mater.*, 2006, **16**, 2324.
- 60 X. Liang, X. Wang, J. Zhuang, Q. Peng and Y. D. Li, *Adv. Funct. Mater.*, 2007, **17**, 2757.
- 61 M. H. Du, S. C. Erwin and A. L. Efros, *Nano Lett.*, 2008, **8**, 2878.
- 62 S. C. Erwin, L. J. Zu, M. I. Haftel, A. L. Efros, T. A. Kennedy and D. J. Norris, *Nature*, 2005, **436**, 91.
- 63 B. M. van der Ende, L. Aarts and A. Meijerink, *Adv. Mater.*, 2009, **21**, 1.
- 64 P. J. Bendall, C. R. A. Catlow, J. Corish and P. W. M. Jacobs, *J. Solid State Chem.*, 1984, **51**, 159.
- 65 D. R. Tallant, D. S. Moore and J. C. Wright, *J. Chem. Phys.*, 1977, **67**, 2897.
- 66 D. Q. Chen, L. Lei, R. Zhang, A. P. Yang, J. Xu and Y. S. Wang, *Chem. Commun.*, 2012, **48**, 10630.
- 67 F. Vetrone, R. Naccache, V. Mahalingam, C. G. Morgan and J. A. Capobianco, *Adv. Funct. Mater.*, 2009, **19**, 2924.
- 68 M. Pedroni, F. Piccinelli, T. Passuello, M. Gioarola, G. Mariotto, S. Polizzi, M. Bettinelli and A. Speghini, *Nanoscale*, 2011, **3**, 1456.
- 69 Y. S. Liu, D. T. Tu, H. M. Zhu, R. F. Li, W. Q. Luo and X. Y. Chen, *Adv. Mater.*, 2010, **22**, 3266.
- 70 F. Wang, R. R. Deng, J. Wang, Q. X. Wang, Y. Han, H. M. Zhu, X. Y. Chen and X. G. Liu, *Nat. Mater.*, 2011, **10**, 968.
- 71 Q. Q. Su, S. Y. Han, X. J. Xie, H. M. Zhu, H. Y. Chen, C. K. Chen, R. S. Liu, X. Y. Chen, F. Wang and X. G. Liu, *J. Am. Chem. Soc.*, 2012, **134**, 20849.
- 72 F. Vetrone, R. Naccache, V. Mahalingam, C. G. Morgan and J. A. Capobianco, *Adv. Funct. Mater.*, 2009, **19**, 2924.
- 73 D. M. Yang, C. X. Li, G. G. Li, M. M. Shang, X. J. Kang and J. Lin, *J. Mater. Chem.*, 2011, **21**, 5923.
- 74 D. Q. Chen, L. Lei, A. P. Yang, Z. X. Wang and Y. S. Wang, *Chem. Commun.*, 2012, **48**, 5898.